



CACAIE

From Adeli, Hojjat <adeli.1@osu.edu>

Date Mon 2024-11-11 17:07

To Fascetti, Alessandro <FASCETTI@pitt.edu>

Cc Brigham, John C <brigham@pitt.edu>; Zhu, Yingbo <YIZ189@pitt.edu>; Jia, Dongge <DOJ14@pitt.edu>

 9 attachments (17 MB)

Wiley Overage and color printing fees authorization form.pdf; CACAIE Cover Image Application.docx; 39-22.pdf; 39-20.pdf; 39-19.pdf; 39-18.pdf; 39-17.pdf; 39-16.pdf; 39-15.pdf;

Re: Coupled Lattice Discrete Particle Model for the simulation of water and chloride transport in cracked concrete members

Yingbo Zhu, Dongge Jia, John C. Brigham, and **Alessandro Fascetti** (USA)

Dear Dr. Fascetti:

I have decided not to send your paper out for another round of review. I am pleased to inform you that your above-referenced-manuscript has been accepted for publication in **Computer-Aided Civil and Infrastructure Engineering**. In the revised paper, the following figures need to be printed in color: Figures 1, 5, 7, 11 and 12. If the color printing fee is a concern, you can combine the adjacent figures as long as they fit one page and the lettering in the figure remains legible (font size of at least 10). It seems to me Figures 11 and 12 can be combined into one Figure 11a and 11b. Please update the attached Wiley form submitted earlier.

The publisher has now included CACAIE in their Cover Sale program. Please see the website: <https://onlinelibrary.wiley.com/page/journal/14678667/homepage/cover-images>. This has become a popular feature as the covers of all 18 issues published in 2023, all 24 scheduled issues of 2024, and the first 7 scheduled issue of 2025 have a Cover Sale. Some of your figures or a combination of them such as Figures 5, 7, 11 and 12. are suitable for Cover Sale. Samples are attached. There is a queue/waiting list for the Front Cover Sale until June 2025 but you may also apply for **Back Cover Sale which can be scheduled earlier**. Please let me know if you are interested to reserve a cover for you. Thank you.

Regards,

Hojjat Adeli, Distinguished Member, ASCE, Fellow, IEEE, AIMBE, AAAS, and American Neurological Association

Academy Professor

The Ohio State University

Editor-in-Chief, **Computer-Aided Civil and Infrastructure Engineering**

RESEARCH ARTICLE**Coupled Lattice Discrete Particle Model for the simulation of water and chloride transport in cracked concrete members****Yingbo Zhu^{1,*} | Dongge Jia^{1,*} | John C. Brigham^{1,2} | Alessandro Fascetti^{1,2}**¹Department of Civil and Environmental Engineering, University of Pittsburgh, Pittsburgh, Pennsylvania, USA²Department of Bioengineering, University of Pittsburgh, Pittsburgh, Pennsylvania, USA

*Co-first authors

Authorship

Yingbo Zhu and Dongge Jia should be considered joint first author.

Correspondence

Alessandro Fascetti, Department of Civil and Environmental Engineering, University of Pittsburgh, 3700 O'Hara Street, Pittsburgh, PA 15261, USA.
Email: fascetti@pitt.edu

Funding information

The findings presented herein are based upon work supported by the Impactful Resilient Infrastructure Science & Engineering (IRISE) consortium in the Department of Civil and Environmental Engineering at the University of Pittsburgh.

ABSTRACT

A novel coupled mechanical and mass transport lattice discrete particle model is developed to quantitatively assess the impact of cracks on the mass transport properties in concrete members subjected to short- and long-term loading conditions. In the developed approach, two sets of dual lattice networks are generated: one to resolve the mechanical response and another for mass transport analysis. The cracks simulated by the mechanical lattice are mapped onto the transport elements to investigate the effect of cracks on the global transport properties in concrete members. A new quantitative relationship is proposed for the estimation of the diffusion coefficient based on local crack information, and the developed model is capable of describing both convection and diffusion mechanisms. Moreover, creep behavior is incorporated to account for the influence of cracks induced by long-term loading conditions. Numerical results, in the form of dynamic changes in cumulative water and chloride contents in concrete members under tension, compression, and bending with various stress levels show remarkable accuracy when compared to available experimental observations. The developed model provides an effective means for incorporating mesoscale information in simulations of water and chloride transport in concrete members under varying short- and long-term loading conditions.

1 | INTRODUCTION

Chloride-induced corrosion in reinforced concrete members has been recognized as one of the most significant reasons for structural deterioration in civil infrastructure. According to a report by the US Federal Highway Administration (Federal Highway Administration, 2002), the annual cost of corrosion for mitigation and rehabilitation related to concrete highway bridges was approximately \$8.3 billion; furthermore, the report estimated that indirect costs to users, such as traffic delays and lost productivity, were up to 10 times the direct corrosion costs. The presence and evolution of cracking in concrete promote faster ingress of aggressive ions from the surface to the interior, affecting both the performance and durability of the concrete itself and reinforcements (Ismail et al., 2004). This intrusion, in turn, can further exacerbate cracking and result in substantial deterioration of concrete, particularly in aggressive environments characterized by

freeze-thaw cycles (Yang et al., 2006). In this context, the complex interactions between mechanical degradation and penetration of aggressive ions pose considerable scientific challenges in the definition of predictive models and computational approaches for the simulation of the coupled effects. Consequently, quantifying the impact of cracking on the transport properties of concrete has been a central focus in civil engineering research over the last two decades.

Cracking is often indicative of the deterioration of concrete components, making its investigation a key focus in civil engineering (Quqa et al., 2023; Ye et al., 2023; Zhou et al., 2023). In the last decades, extensive experimental research has been conducted in this field to quantitatively characterize the influence of cracking on transport characteristics. For example, Dehghan et al., 2017 and Marsavina et al., 2009 adopted the artificial method to create desired cracks at prescribed locations in concrete members, allowing for easy quantification of the influence of crack width and length. To overcome the limitations associated with artificially inducing

cracks and gain a deeper understanding of the global transport properties of cracked concrete members, considerable investigations have been performed on concrete specimens with mechanically-induced cracks subjected to different types of loadings with varying stress levels, such as tension (Jang et al., 2011; J. Wang et al., 2016), compression (Djerbi Tegguer et al., 2013; Rahman et al., 2012), and 4-point bending (Şahmaran, 2007; Y. S. Zhang et al., 2011).

At the same time, computational methods are valuable tools to complement experimental tests and to enable deeper understanding of the underlying physical processes (Zhu et al., 2024) by means of deterministic (Hafezolghorani et al., 2022) and data-based approaches (Rafiei et al., 2016, 2017b, 2017a). Several works employed the finite element method (FEM) to investigate chloride transport processes through models of concrete at the mesoscopic scale, explicitly describing aggregate particles, the matrix, and interfacial transition zone. For example, available works (Bentz et al., 2013; Peng et al., 2019; Qiu & Dai, 2021) presented 2D multi-phase concrete models with user-defined cracks to study the influence of crack width and height on chloride transport (CLT) properties. Abyaneh et al., 2016 reported a 3D two-phase concrete model with randomly placed microcracks at the interface between aggregate and matrix to explore the effect of microcrack widths on CLT properties.

To address the limitations of using user-defined cracks in the simulations, coupled FEM analyses have been proposed recently. Li & Guo, 2020 applied peridynamics to the simulation of the crack evolution of 2D multi-phase concrete members under various types of external loading, with the goal of investigating the effects of crack networks on chloride penetration. Similar work was undertaken by Q. Liu et al., 2022, where crack propagation in a 2D model under tension was captured by means of the extended finite element method. To achieve a more realistic representation of cracks, a 3D concrete model, reflecting the morphology of real aggregates, was built by using the spherical harmonic theory (Zheng et al., 2022), and then the cracks captured by a damage constitutive law were used to analyze the CLT properties. More recently, Tong et al., 2024 simulated realistic 3D microstructures to investigate CLT in concrete. Although FEM is widely adopted and has been extensively validated (Adeli & Kumar, 1995; Yu & Adeli, 1993), its application to simulating coupled nonlinear mechanical response and mass transport brings significant challenges in capturing local mesoscale features that are inherent in concrete as a result of its heterogeneous nature.

Another viable alternative for simulating the mass transport process in concrete materials is the adoption of discrete methods based on a lattice modeling approach (Grassl, 2009; Šavija et al., 2013). The lattice elements serve as idealized conduits for mass transport, providing a mesoscale framework for flow analysis in cementitious composites. In the early stages, lattice models were employed to simulate flow permeability and water absorption in cracked concrete

members (Grassl, 2009). Further advancements extended capabilities of the approach to simulate the CLT process in cracked concrete members (Šavija et al., 2013, 2014). Although the developed model exhibited good agreement with experimental results, it did not consider the nonlinear mechanical behavior of the material. More recent works (L. Wang et al., 2016) investigated both the chloride diffusion and convection mechanism on the CLT based on a 2D lattice network model with prescribed cracks. Tran et al., 2021 developed a 2D mesoscale mechanical-transport lattice network model to simulate the water and chloride diffusion properties of concrete subjected to compressive loading. However, the flexibility of this model is limited by the introduced compressive damage variable to characterize the degree of damage in the material. This is primarily because material under volumetric compression exhibits hardening behavior.

Recent research (Shen et al., 2020) presented a coupled hygro-thermal LDPM formulation to simulate thermal spalling in concrete, investigating the effect of cracks on the mass transport and heat transfer under high temperatures. Y. Zhang et al., 2021 presented a multi-physics lattice model capable of accounting for thermal and hygral effects on CLT in non-saturated cementitious composites. In this model, a transport lattice network topology was proposed based on the LDPM tetrahedralization. However, this work did not consider the effect of cracking on the transport process in concrete. Furthermore, the Flow Lattice Model was recently extended to simulate chloride intrusion in ultra-high-performance concrete (Cibelli et al., 2023). Similarly, Yin et al., 2024 proposed a Flow Lattice Model by including Hygro-Thermo-Chemical effects, to simulate the moisture and heat transport process in concrete materials. These models have been proven to be able to realistically describe coupled hygro-thermo-chemical effects in concrete under a variety of loading and environmental conditions, generally providing a computationally efficient avenue to simulate material behavior while explicitly considering mesostructural information.

The numerical investigations into the effect of loading-induced cracks on the CLT in concrete are limited, due to the significant challenges associated with the description of the complex multi-physical aspects of the phenomenon. The first challenge lies in the integration of mechanical and transport models. Although some coupled mechanical-transport models were presented in the literature, these models are typically tailored to specific loading scenarios. Concrete structures, however, can suffer damage from various types of loads, and the numerical models need to provide flexibility and generalizability to allow for robust predictions. Second, modeling CLT in unsaturated concrete poses several complexities. The transport process involves convection dominating the early stages, followed by diffusion-dominated effects once the concrete is saturated. The water content is a key parameter that influences the velocity of chloride

intrusion, while the majority of available models neglect the convective effects induced by capillary absorption. The third challenge is related to the quantification of the effects of damage/cracks caused by long-term loading on the CLT. Long-term loadings contribute to damage evolution in concrete members, potentially leading to substantial crack propagation. Such processes can create preferential pathways and channels for fluid and ion ingress and, in turn, cause further damage. Another significant challenge is how to quantify the influence of microcracks distributed throughout the entire specimen on global diffusion properties. Concrete is a highly heterogeneous material that can develop not only visible main cracks but also numerous microcracks (which cannot be observed by the naked eye) that significantly affect CLT properties. Previous research predominantly concentrates on the impact of main cracks or user-defined cracks on the local diffusion characteristics within the vicinity of these cracks while overlooking the influence of microcracks.

To overcome the aforementioned challenges, a coupled LDPM approach is presented in this study to assess the effects of cracking on the transport properties in concrete members subjected to various types of short- and long-term loadings. Fundamental novelty presented in this study and major contributions can be summarized as follows:

- (1) A novel LDPM approach is proposed for coupled mechanical and water-chloride transport simulations. The mechanical lattice is used to simulate the nonlinear behavior of concrete members, after which a second lattice network model is constructed and exercised to analyze the mass transport properties in concrete members by mapping crack information onto the transport elements. The transport lattice elements are constructed to be parallel to crack planes, as idealized in the mechanical lattice elements. Each tetrahedron in the mechanical lattice network is used to generate 4 transport lattice elements, resulting in a dense discretization of the transport phenomena.
- (2) The developed approach incorporates creep behavior in the coupled simulations, providing comprehensive insights into the effect of long-term loading on the CLT properties of concrete elements.
- (3) An exponential formulation for estimating the local chloride diffusivity in the presence of microcracks is proposed, which allows for assessing concrete components with various stress levels.
- (4) Water capillary absorption is incorporated in the coupled model, facilitating consideration of both convection and diffusion of CLT in unsaturated concrete.

The organization of this paper is as follows: Section 2 introduces the principles of the proposed approach and the framework for water and chloride transport analysis. Section 3 details the numerical implementation for coupling the mechanical and transport responses. Section 4 presents a water transport analysis of concrete under compressive and tensile actions. Section 5 presents results of numerical

investigations on chloride transport in concrete under both short-term compressive loading and long-term four-point bending. Section 6 presents additional results to validate the robustness and reliability of the model, as well as explores the effects of relative water content and creep behavior on chloride transport in concrete. Lastly, the key conclusion and limitation of this study are summarized in Section 7.

2 | COUPLED MECHANICAL AND MASS TRANSPORT LDPM

2.1 | Dual lattice network topology

In the developed coupled LDPM, the canonical two-phase mesoscale structure of concrete is considered, consisting of coarse aggregates and mortar paste. As is customary, the lattice system for the mechanical modeling is constructed by randomly placing in the domain poly-sized spheres representing the given particle size distribution in the material, a Delauney tetrahedralization for the particle centroids, and a centroidal LDPM tessellation, as described in Figures 1(a-d). The details of the generation of aggregate particles, mechanical lattice networks and calibration process can be found in the literature (Cusatis et al., 2011). In addition, it should be noted that the constitutive laws used in the mechanical model were derived from previous work from the co-authors (Fascetti et al., 2018; Zhu & Fascetti, 2024) and slightly differ from the original work by Cusatis et al. (2011).

In contrast to the mechanical lattice elements, which connect a pair of adjacent aggregates, transport elements are defined around the volume of the aggregate particles, under assumption of aggregate conductivity being significantly lower than that of the mortar. The transport network is generated by leveraging the canonical LDPM tessellation (Cusatis et al., 2011), as follows (see Figure 1(f)): the effective volume centroid T is defined as the point at which all contact facets in a tetrahedron intersect, while the points F_i ($i = 1, 2, 3, 4$) are defined as the centroids of each surface of the tetrahedron. The transport lattice elements in each tetrahedron are obtained by connecting points T and F_i (i.e., $\overline{TF_1}$, $\overline{TF_2}$, $\overline{TF_3}$, $\overline{TF_4}$), as shown in Figure 1(f), resulting in 4 transport lattice elements per tetrahedron. By employing such tessellation, the transport lattice elements retain the fundamental property of being parallel to the potential crack planes, as idealized in the construction of the mechanical lattice network. (see Figure 1(h)). For this reason, the influence of local cracks on mass transport can be described in a discrete fashion, this being one of the significant features of the coupled LDPM approach developed herein.

The proposed coupled LDPM offers several key advantages over traditional FEM for simulating the transport behavior of concrete under external loading. Unlike FEM, which faces challenges in accurately characterizing the geometry of each material phase, LDPM is a mesoscale model that integrates detailed mesostructural information, allowing

it to effectively simulate complex nonlinear behavior in a computationally efficient fashion. Moreover, by aligning transport elements with the cracks defined in the mechanical lattice, the coupled LDPM provides a feasible approach to investigate the influence of local cracks on mass transport—something that is difficult to achieve with traditional FEM.

In addition, it is worth noting that the concept of a transport lattice network in this study is similar to that of the previous works (Cibelli et al., 2023; Yin et al., 2024; Y. Zhang et al., 2021), while the main difference lies in the definition of the transport elements. Previous works defined the transport network as the connection between adjacent tetrahedra centroids, whereas this approach herein adopts a denser lattice by connecting the volume centroid of each tetrahedron to the centroids of its surfaces, as detailed in the previous. Such denser lattice allows for mesostructural features to be directly represented in the idealization of CLT in concrete elements.

2.2 | Mechanical LDPM with creep behavior

2.2.1 | Strain compatibility

In LDPM simulations, each particle is assumed to undergo rigid body motion. The displacement jump ($[[\mathbf{u}]]$) at the centroid of each resisting area (point C in Figure 1(d)) can therefore be expressed by:

$$[[\mathbf{u}]] = \mathbf{u}^J - \mathbf{u}^I + \boldsymbol{\theta}^J \times \mathbf{C}^J - \boldsymbol{\theta}^I \times \mathbf{C}^I \quad (1)$$

Based on such measure, the strain (ε_α) and curvature (κ) in each lattice element is obtained as:

$$\begin{cases} \varepsilon_\alpha = \frac{[[\mathbf{u}]]}{l_e} \cdot \mathbf{e}_\alpha \\ \kappa = \frac{(\boldsymbol{\theta}^J - \boldsymbol{\theta}^I)}{l_e} \cdot \mathbf{e}_\alpha \end{cases} \quad (2)$$

where \mathbf{u}^I , $\boldsymbol{\theta}^I$ and \mathbf{u}^J , $\boldsymbol{\theta}^J$ are the translation and rotation vectors at Node I and Node J , respectively; \mathbf{C}^I and \mathbf{C}^J are the vectors connecting Nodes I and J to the Centroid C ; \mathbf{e}_α is the unit vector that defines the local coordinates of each lattice strut, $\alpha = n, l, m$; l_e is the length of the lattice element.

In structural applications, CLT in concrete components is a process that evolves at larger temporal scales than mechanical damage (Abdellatif et al., 2019; Di Luzio & Cusatis, 2013). Therefore, in order to capture degradation mechanisms in a coupled framework, it is essential to consider the creep response of concrete in the analyses. While shrinkage does contribute to cracking in concrete, it primarily influences volumetric deformation during the initial curing and drying stages (Dellinghausen et al., 2012), with its effects reducing over time. Given that all the experiments on chloride transport used in the following only focused on the effects of loading durations on the resulting transport properties of concrete members, with shrinkage generally not considered/measured, this study focuses on investigating the effects of external loading (both short- and long-term) on mass transport, therefore neglecting shrinkage effects in the simulations.

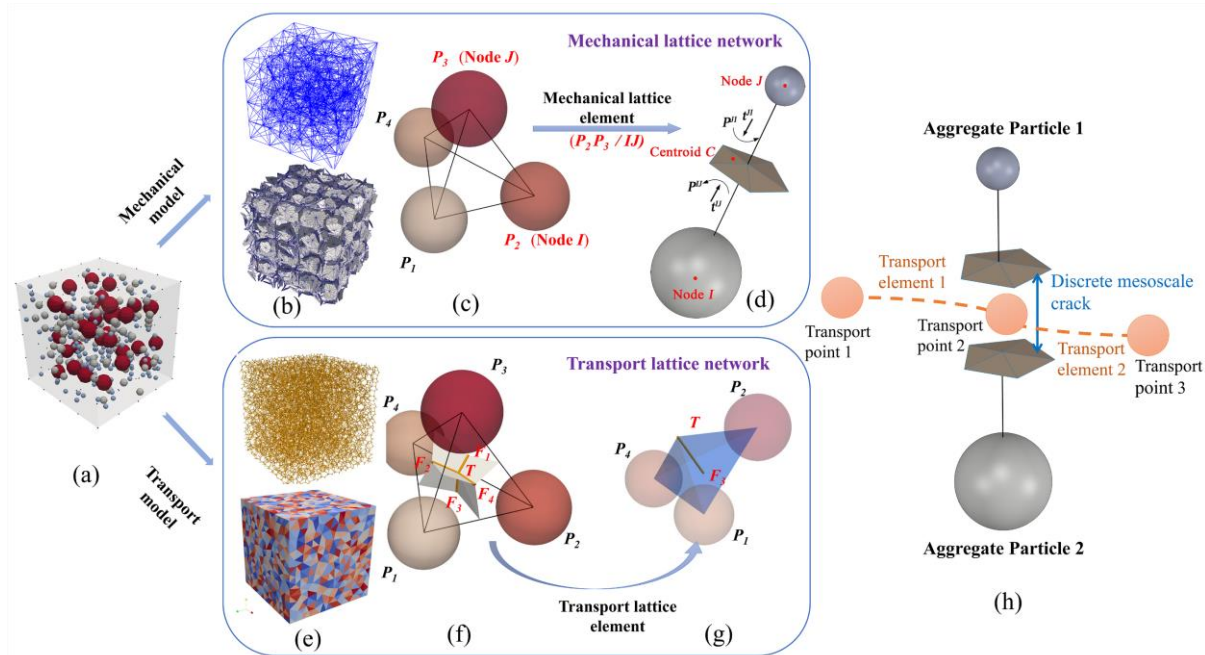


FIGURE 1 Dual lattice network topology: (a) random placement of particles; (b) mechanical lattice struts and facets; (c) tetrahedron consisting of particles and lattice struts; (d) a lattice element; (e) transport lattice network and transport cells; (f) transport lattice element dual to the Delaunay; (g) transport lattice element and the volume it represents; (h) idealized flow paths parallel to the crack plane.

Herein, the total facet strain rate of each lattice element under long-term loading conditions is estimated by the

addition of the short-term strain rate $\dot{\varepsilon}_{\alpha,ed}$ and the creep strain rate, which is composed by the viscoelastic strain rate $\dot{\varepsilon}_{\alpha,ve}$

and purely viscous strain rate $\dot{\varepsilon}_{\alpha,v}$:

$$\dot{\varepsilon}_{\alpha} = \dot{\varepsilon}_{\alpha,ed} + \dot{\varepsilon}_{\alpha,ve} + \dot{\varepsilon}_{\alpha,v} \quad (3)$$

The viscoelastic strain rate and the purely viscous strain rate is defined as (Abdellatef et al., 2019; Bazant & Prasannan, 1989a; Bažant & Prasannan, 1989b):

$$\begin{cases} \dot{\varepsilon}_{\alpha,ve} = \frac{1}{v(\alpha_b)} \dot{\gamma} \\ \dot{\varepsilon}_{\alpha,v} = \xi \kappa \phi S G \sigma_{\alpha} \end{cases} \quad (4)$$

where $v(\alpha_b)$ represents the binder volume fraction produced by chemical reaction at early age and $\dot{\gamma}$ is the viscoelastic micro-strain rate of the binder; ξ and κ are model parameters, ξ is usually determined by calibrating models with experimental results (unit: MPa^{-1}), and κ is assumed as $2 \times 10^{-8} (\text{MPa} \cdot \text{day})^{-1}$; $\phi = (0.1 + 0.9h^2) \exp(Q_s/R(1/T_0 - 1/T))$ is an environmental parameter associated with temperature T , h is the relative humidity and $Q_s/R \approx 5000$ °K. For all analyses herein, the temperature T is set equal to the reference room temperature T_0 ; S is the microprestress calculated by solving the differential equation $\dot{S} + \phi \kappa S^2 = \kappa_1 [\dot{T} \ln(h) + T \dot{h}/h]$; κ_1 is a model parameter related to the drying viscous behavior; σ_{α} is the traction acting on the lattice strut, which only accounts for the short-term strain of $\varepsilon_{\alpha,ed}$; $G = 1$ if $\alpha = n$ and $G = 1/\vartheta$ if $\alpha = l, m$; $\vartheta = (1 - 4\nu)/(1 + \nu)$ is a shear-normal coupling parameter for lattice elements at the mesoscopic scale, which is related to the macroscopic Poisson's ratio ν .

It is worth noting that preliminary numerical observations conducted by the authors suggested that the effect of viscoelastic aging is significantly less pronounced than that of purely viscous aging for all the tests reported herein. This finding is in substantial agreement with conclusions reported in (Bazant & Prasannan, 1989b), which concluded that the viscous strain rate is predominant when considering sustained loading conditions at a relatively early age (which is the case for the experimental tests simulated herein). Therefore, for the sake of minimizing calibration parameters, the value of the viscoelastic strain rate was assumed to be negligible in all the simulations reported in the following.

2.2.2 | Constitutive laws

To simulate inelastic behavior, an elliptical stress boundary surface is employed (Fascetti et al., 2018):

$$\begin{cases} \sigma(\omega) = \frac{\sin \omega (f_c + f_t) + \sqrt{D}}{2 \left(\sin \omega^2 - \frac{\cos \omega^2 \vartheta f_c f_t}{f_s^2} \right)} \\ D = [\sin \omega (f_c + f_t)]^2 - 4 f_c f_t (\sin \omega^2 - \cos \omega^2 \vartheta f_c f_t / f_s^2) \end{cases} \quad (5)$$

where $\sigma = \sqrt{\sigma_n^2 + \sigma_t^2/\vartheta}$ and $\varepsilon = \sqrt{\varepsilon_n^2 + \vartheta \varepsilon_t^2}$ are defined as the effective traction and strain measures, respectively; $\omega = \arctan(\varepsilon_n/\sqrt{\vartheta} \varepsilon_t)$ is the coupling strain.

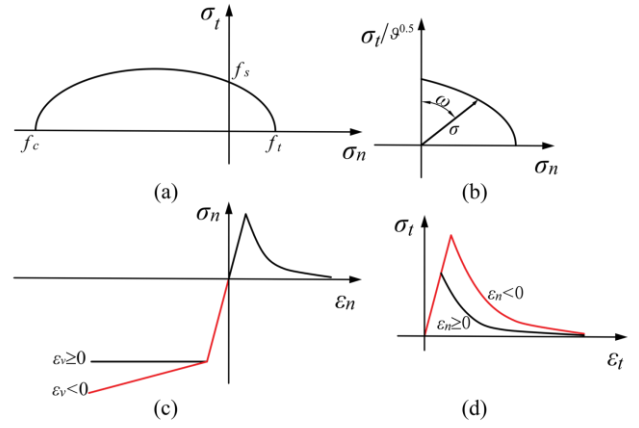


FIGURE 2 Constitutive laws adopted for the mechanical lattice: (a) elliptical bounding surface of $\sigma_n - \sigma_t$ curves; (b) parameter w in terms of σ_n and σ_t ; (c) compressive and tensile behavior; (d) shear behavior.

The nonlinear constitutive laws for each lattice element are defined in terms of three different stress-strain conditions: (1) cohesive behavior due to tension and shear; (2) hardening behavior under multi-axial compression; and (3) frictional behavior resulting from interacting compressive and shear actions. A brief illustration of the constitutive laws is given in Figures 2(c)-(d), while the essential equations are summarized in the Appendix. As previously mentioned, the nonlinear constitutive laws used in this study differ from those in the original LDPM formulation (Cusatis et al., 2011). For the full details on the constitutive relationships employed herein, the reader is referred to previous works by the co-authors (Fascetti et al., 2018, 2022; Jia et al., 2024).

2.3 | Mass transport model

The CLT mechanism in the early transport stage (i.e., before saturation of concrete components) is predominantly convective, as a result of capillary absorption. This stage is followed by diffusion-dominated behavior, once the concrete approaches full saturation. In addition, the chloride diffusion properties are significantly influenced by the water content in unsaturated concrete (de Vera et al., 2007; Y. Zhang et al., 2018). To this end, all the aforementioned aspects (i.e., water transport and chloride diffusion) need to be described by numerical models.

2.3.1 | Water transport

The Richards' equation derived from Darcy's law and the mass conservation law for unsaturated flow within porous material is expressed as (Lockington et al., 1999):

$$\frac{\partial \theta}{\partial t} = \frac{\partial}{\partial x} \left(D_w(\theta) \frac{\partial \theta}{\partial x} \right) \quad (6)$$

where θ is the relative water content, defined as $\theta = \frac{\theta - \theta_i}{\theta_s - \theta_i}$; θ_i and θ_s are the water contents at the current stage, its reference value at the start of the simulations, and at complete saturation, respectively; D_w is the water diffusivity

coefficient, which is a material property influenced both by the material mixture and the relative water content. Previous works (Hall, 1989; Lockington et al., 1999) proposed an exponential law to estimate diffusivity in unsaturated concrete in the absence of mechanical damage:

$$D_w(\theta) = D_{w,0} e^{n\theta} \quad (7)$$

where n is an empirically estimated constant representing the shape of diffusivity curves (typically, $n = 6 \sim 9$), while $D_{w,0}$ is the value of the diffusion coefficient in dry conditions. Since direct measurement of $D_{w,0}$ is challenging, its value is usually estimated from the material's sorptivity S (Lockington, 1993; Lockington et al., 1999), as shown in Equation (8). Additionally, experimental findings (L. Wang & Li, 2014; Yang et al., 2006) have shown that the initial water absorption (first 2~4 hours) is larger than that observed at later stages. Therefore, this study proposed the use of a scaling parameter ρ ($\rho = 2.5$ for all analyses shown herein) describing this mechanism:

$$D_{w,0} = \begin{cases} \frac{1}{123.13} \left(\frac{S}{\theta_s - \theta_i} \right)^2, & t < 120 \text{ min} \\ \frac{1}{123.13\rho} \left(\frac{S}{\theta_s - \theta_i} \right)^2, & t \geq 120 \text{ min} \end{cases} \quad (8)$$

The effect of a crack on diffusivity is accounted for by incorporating the quadratic element law for water flow in a crack, which is given as:

$$D_w(\theta, w_c) = \left(D_{w,0} + \frac{w_c^2 p_r}{12\eta} \right) e^{n\theta} \quad (9)$$

where w_c is the crack width; η is the viscous dynamic coefficient of water (0.001 Pa·s); p_r is the reference pressure, determined as 18.62 N/mm² by fitting with the experimental capillary curves for ordinary Portland cement (OPC) (L. Wang et al., 2016). Moreover, the value of $D_w(\theta, w_c)$ is capped at the value of 1 in the numerical models, to avoid unrealistically large values resulting from extremely large cracks.

2.3.2 | Chloride transport

CLT in unsaturated concrete, considering both the convection and diffusion effects, can be described by:

$$\frac{\partial C_t}{\partial t} = \nabla \cdot (D_{cl}(\theta) \nabla C_f) + C_f \frac{\partial \theta}{\partial t} \quad (10)$$

where D_{cl} is the chloride diffusivity coefficient; $C_t = C_f + C_b$ is the total chloride concentration, consisting of the free concentration C_f and bound chloride concentration C_b . By introducing the chloride binding capacity $\lambda = \partial C_b / \partial C_f$, the change of chloride concentration with time can be expressed as:

$$\frac{\partial C_t}{\partial t} = \frac{\partial C_f}{\partial t} + \frac{\partial C_b}{\partial t} = (1 + \lambda) \frac{\partial C_f}{\partial t} \quad (11)$$

The chloride binding capacity λ is a material property, which can be expressed as (Xi & Bažant, 1999):

$$\lambda = 10^B \frac{A_0 \beta_{gel}}{35450 \beta_{sol}} \left(\frac{C_f}{35.45 \beta_{sol}} \right)^{A_0 - 1} \quad (12)$$

where A_0 and B are material constants, 0.38 and 1.14 for OPC, respectively; β_{sol} is the ratio of pore solution to concrete, measured in liters of pore solution per gram of concrete (L/g), and β_{gel} is the ratio of C-S-H gel to concrete, in terms of grams of C-S-H gel per gram of concrete (g/g). The values of β_{sol} and β_{gel} can be determined from the water-to-cement ratio and the specific mix proportion.

At the 1-dimensional level of the transport lattice elements, the CLT process is described by the following governing equation, obtained from combining Equations (10) and (11):

$$\frac{\partial C_f}{\partial t} = \underbrace{\frac{C_f}{1 + \lambda(C_f)} \frac{\partial}{\partial x} \left(D_w(\theta) \frac{\partial \theta}{\partial x} \right)}_{\text{Convection}} + \underbrace{\frac{1}{1 + \lambda(C_f)} \frac{\partial}{\partial x} \left(D_{cl}(\theta) \frac{\partial C_f}{\partial x} \right)}_{\text{Diffusion}} \quad (13)$$

The exponential law for determining the chloride diffusivity D_{cl} in unsaturated concrete material, as proposed in the literature (Saeki & Niki, 1996; L. Wang & Ueda, 2014), is employed herein:

$$D_{cl}(\theta) = D_{cl,0} 0.0032 \times 10^{2.5\theta} \quad (14)$$

where $D_{cl,0}$ is the chloride diffusivity in the saturated concrete in the absence of cracking.

Two empirical relationships (Djerbi Teggner et al., 2013; Šavija et al., 2013) have been proposed in the past to quantify the influence of the crack width (w_c) on the chloride diffusivity caused by cracking ($D_{cl,d}$) based on experimental or numerical calibration results. The primary limitation of these relationships is that they estimate changes in local diffusivity in concrete with large crack widths while ignoring the influence of small cracks and microcracks. However, cementitious materials have been proven to form considerable microscopic crack networks, which are generally undetectable by the naked eye, even under low magnitude loading conditions. These microcracks can significantly increase the global diffusion properties of materials by creating more transport conduits and changing the local porosity. This assumption has been verified in the literature, with several experimental observations (Lim et al., 2000; J. Liu et al., 2017; L. Zhang et al., 2014) reporting that the CLT velocity in concrete members under low tensile/compressive stresses for which no obvious cracks were observed exhibited significant increases when compared with that of the unstressed specimens. To address this challenge, this study proposes a new relationship for accounting for the change diffusivity induced by both micro- and macro-cracks in the domain:

$$D_{cl,c}(\theta, w_c) = \begin{cases} D_{cl}(\theta)e^{aw_c}, & w_c < 10\mu\text{m} \\ D_{fc}, & w_c \geq 10\mu\text{m} \end{cases} \quad (15)$$

where $D_{cl,c}$ is chloride diffusivity for damaged material; the parameter $a = \exp(D_{fc}/D_{cl}(\theta))/10$ for the sake of achieving a smooth transition between the two-phase relationship; D_{fc} is the constant diffusivity value associated with macroscopic cracks (i.e., $w_c \geq 10\mu\text{m}$), and it is calibrated as $D_{fc} = 2.8 \times 10^{-10} \text{ m}^2/\text{s}$ in this study, and will be validated later. **It should be noted that the primary aim of this study is to analyze diffusive and convective transport mechanisms—which are deemed to be the primary contributions to CLT. Other mechanisms, such as ionic charge in the dissolved chlorides, are therefore neglected herein.**

3 | NUMERICAL IMPLEMENTATION

3.1 | Discretization of the mass transport model

The governing equations for water and chloride transport analysis are similar in form, both requiring discretization in spatial and temporal domains. To avoid redundancy, only the discretization process for the water transport equation is described herein. Employing the Galerkin weighted residual method and substituting the spatial discretization into the governing equation of Equation (6) yields a discrete form for water transport analysis for each element (Fascetti & Oskay, 2019; Z. Wang et al., 2024):

$$\mathbf{M}_e \frac{d\theta}{dt} + \mathbf{K}_e(\theta_e)\theta - \mathbf{f}_e = \mathbf{0} \quad (16)$$

where \mathbf{K}_e and \mathbf{M}_e are the diffusivity and mass matrices, respectively; \mathbf{f}_e is the forcing vector; θ_e is the relative water content of a transport lattice element, which is calculated by averaging the relative water content at its two nodes. The form of the elemental matrices is given by (Fascetti & Oskay, 2019; Grassl & Bolander, 2016):

$$\begin{aligned} \mathbf{K}_e &= \int_{\Omega^e} \mathbf{B}^T D_w(\theta_e) \mathbf{B} d\Omega^e \\ &= \xi_1 \int_{l_e} D_w(\theta_e)(x) A_e(x) \mathbf{B}^T \mathbf{B} dx = \frac{\xi_1 D_w(\theta_e) A_e^*}{3l_e} \begin{bmatrix} 1 & -1 \\ -1 & 1 \end{bmatrix} \end{aligned} \quad (17)$$

$$\begin{aligned} \mathbf{M}_e &= \int_{\Omega^e} \mathbf{N}(x)^T \mathbf{N}(x) d\Omega^e \\ &= \xi_2 \int_{l_e} (x) A_e(x) \mathbf{N}(x)^T \mathbf{N}(x) dx = \frac{\xi_2 A_e^* l_e}{30} \begin{bmatrix} 1 & 1.5 \\ 1.5 & 6 \end{bmatrix} \end{aligned} \quad (18)$$

$$\mathbf{f}_e = - \int_{\Gamma_q^e} \mathbf{q} \mathbf{N}^T(x) d\Gamma_q^e = \begin{bmatrix} 0 \\ -q_L A_e^* \end{bmatrix} \quad (19)$$

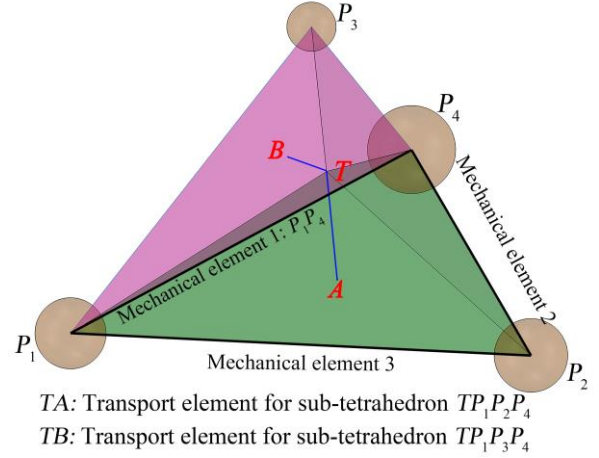


FIGURE 3 Diagram of the crack mapping between mechanical and transport lattice elements.

The evaluation of the cross-sectional area requires special treatment in view of the fact that the transport elements are non-prismatic. To this end, A_e^* is defined as the cross-sectional area at the endpoint of a transport lattice element (i.e., the area formed by points $P_1P_2P_4$ for the transport element \overline{TA} , see Figure 3); the volume centroid T is defined as the starting point of a transport element, while the ending point is the surface point (e.g., points A and B in Figure 3); $A_e(x) = A_e^*(x - x_A)^2/l_e^2$ is the cross-sectional area at an arbitrary point along the length of the transport lattice element, and x is the curvilinear abscissa associated with the element.

Following the assumption that the diffusivity of the coarse aggregate particles is negligible when compared to that of the mortar, the cross-sectional area of each transport element should not include the volume occupied by particles. To this end, volume reduction factors ξ_1 and ξ_2 are introduced in the element diffusion and mass matrices to account for the presence of aggregates. Since the components of the diffusion matrix are of the same order as the element length, the volume reduction factor ξ_1 for \mathbf{K}_e is defined as $\xi_1 = (1 - v_{ae})^{1/3}$, where v_{ae} is the volume fraction of aggregate in the mix. Alternatively, the components of the mass matrix are of the same order as the elemental volume, therefore, the ξ_2 for \mathbf{M}_e is defined as $\xi_2 = 1 - v_{ae}$.

Discretization in time is performed by means of the Crank-Nicolson scheme, which is an unconditionally stable method subject to a maximum time stepping criterion (Fascetti & Oskay, 2019):

$$\left[\frac{\mathbf{K}_e^{t+\Delta t}}{2} + \frac{\mathbf{M}_e}{\Delta t} \right] \theta(t + \Delta t) = \left[-\frac{\mathbf{K}_e^t}{2} + \frac{\mathbf{M}_e}{\Delta t} \right] \theta(t) - \frac{(\mathbf{f}_e^{t+\Delta t} + \mathbf{f}_e^t)\Delta t}{2} \quad (20)$$

$$\Delta t_{max} = \frac{l_{e,min}^2}{2D_w} \quad (21)$$

where Δt_{max} is the maximum time step and $l_{e,min}$ is the minimum length of transport lattice elements in the domain.

3.2 | Coupling and algorithmic procedure

Figure 4 graphically depicts the algorithm utilized in the presented coupled LDPM approach. To perform the transport analyses, the water and chloride concentrations at the nodes on the exposed surface are imposed according to the experimental protocols. For all other nodes within the domain, a user-defined small values (e.g., 0.01 for water and 0.1% for chloride) are assigned to initiate the computation. In the transport simulations, the diffusivity coefficients for water and chloride transport in undamaged concrete need to be measured or determined first, while the values in presence of cracks are evaluated by means of the proposed formulation, as described in Equations (9) and (15).

In the algorithm, a central difference scheme is utilized to integrate the equation of motion, while Crank-Nicolson method is used for the mass transport analysis, as described in the previous. Moreover, when modeling the mechanical response of concrete under short-term loading, a displacement-control scheme is used to capture the nonlinear strain-softening behavior. In contrast, for long-term loading conditions, a force-control scheme is employed to simulate the structural behavior under sustained loads. Based on Equation (4), the purely viscous strain at time t ($\varepsilon_{\alpha,v}^t$) can be calculated by:

$$\varepsilon_{\alpha,v}^t = \varepsilon_{\alpha,v}^{t-\Delta t} + \Delta t \xi \kappa \phi S^t G \sigma_{\alpha}^{t-\Delta t} \quad (22)$$

$$S^t = S^{t-\Delta t} - \phi_s \kappa (S^{t-\Delta t})^2 \Delta t + \kappa_1 \left[\Delta T \ln(h) + \frac{T \Delta h}{h} \right] \quad (23)$$

where $\varepsilon_{\alpha,v}^{t-\Delta t}$ is the viscous strain at the previous step; S^t and $S^{t-\Delta t}$ are the microprestresses in the mechanical lattice elements at the current and previous step, respectively.

The crack width in each mechanical lattice element (w_{mech}) is calculated as follows (Fascetti et al., 2018):

$$w_{mech} = \sqrt{w_n^2 + w_t^2} \quad (24)$$

where $w_n = l_e(\varepsilon_n - \sigma_n/E_n)$ and $w_t = l_e(\varepsilon_t - \sigma_t/E_t)$ are the normal and tangential crack openings, respectively; for short-term loading conditions $\varepsilon_n = \varepsilon_{n,ed}$ and $\varepsilon_t = \varepsilon_{t,ed}$, while for long-term loading conditions $\varepsilon_n = \varepsilon_{n,ed} + \varepsilon_{n,v}$ and $\varepsilon_t = \varepsilon_{t,ed} + \varepsilon_{t,v}$.

As shown in Figure 3, each transport element is associated with three mechanical lattice elements in space. Therefore, the crack width of each transport element can be estimated by mapping the crack widths of the three mechanical lattice elements onto the transport element. This choice results in a one-way coupling between the mechanical damage simulated on the mechanical lattice and the transport properties of the dual lattice. To perform such coupling, a procedure conceptually similar to the mapping of local damage in dual lattices, as proposed in Z. Wang et al., 2024, is adopted herein. Taking the transport element \overline{TA} as an example, the mapped crack width ($w_{trans,TA}$) can be calculated by:

$$w_{trans,TA} = \sum_{i=1,2,3} w_{mech,iA} \quad (25)$$

$$w_{mech,ij} = w_{mech,i} * \frac{V_j}{V_A + V_B} \quad (26)$$

where $w_{mech,ij}$ ($i = 1,2,3, j = A,B$) is the crack width value mapping from the mechanical element i to the corresponding transport elements \overline{Tj} ; $w_{mech,i}$ is the crack width in the mechanical element i ; V_A and V_B are the volumes of the sub-tetrahedra $TP_1P_2P_4$ and $TP_1P_3P_4$ for the transport elements \overline{TA} and \overline{TB} , respectively.

3.3 | Calibration

Calibration of the mechanical parameters associated with the short-term loading conditions (i.e., the standard LDPM formulation) was conducted by matching numerical predictions to the peak strength and stiffness reported in the selected experimental works. The parameters associated with the viscous effects (such as κ , ϕ , and Q_s/R in Equations (22)-(23)) were set to be equal to the values reported in literature (Abdellatef et al., 2019), in view of the fact that no experimental measures were reported in the selected tests. Lastly, the transport model presented herein requires calibration of the coefficients $D_{cl,0}$, $D_{w,0}$, and λ . The parameter λ was estimated by means of the expression proposed by Xi & Bazant (1999), as presented in Section 2.3.2. The values of chloride and water diffusivity (i.e., $D_{cl,0}$ and $D_{w,0}$) were directly obtained from the experimental tests, therefore requiring no additional calibration.

4 | NUMERICAL RESULTS FOR WATER TRANSPORT

4.1 | Water transport of concrete under compression

Wang & Li, 2014 report a series of tests that explored the effect of microcracks on water absorption in concrete under tensile and compressive loading conditions with varying stress levels. The uniaxial compressive (f_c) and tensile (f_t) strengths of the concrete specimens with size $100 \times 100 \times 200$ mm were reported as 41.2 ± 3.2 MPa and 3.6 ± 0.3 MPa, respectively. In the first set of tests, uniaxial compression with stress levels of $0.7 \sim 0.9 f_c$ was applied to concrete specimens to induce microcracks. Then, the specimens were sliced to obtain three sub-specimens of size $100 \times 100 \times 50$ mm. After initial testing, the sub-specimens were oven dried. To ensure a controlled water flow direction, the top surface and the four lateral sides of each sub-specimen were sealed, leaving only the exposed bottom surface open to water transport mechanisms. This configuration allowed for one-way water flow from the bottom to the top (along the loading direction) during the immersion test, as indicated in

Figure 5(b). The three sub-specimens were labeled based on their original positions in the prismatic specimens, as follows: T (top), M (middle), and B (bottom). To speed up the computations, one quarter of the specimen is simulated with the developed approach (see Figure 5(a)). On the mechanical lattice network, the bottom and top nodes were fully fixed, so that all the associated degrees of freedom (i.e., translations and rotations) were restrained. Additionally, the top nodes were assigned the corresponding loading conditions, thorough either displacement- or force-controlled schemes. The concrete material properties employed in the mechanical LDPM simulations are summarized in Table 1.

Figure 5(b) shows that the mechanical model captures a compressive strength of 42.29 MPa, closely aligning with the experimental average value. Figures 5(c)-(d) report the simulated crack patterns and the distributions of crack widths in the concrete at different stress levels, which exhibits the expected significant increase in crack number and width with increasing stress level.

The transport lattice network model was then generated based on the mesh configuration of the mechanical LDPM, with crack widths calculated in the mechanical model mapped to the transport lattice elements using the methodology described in the previous. For water transport analysis, the relative water content for the bottom nodes in the transport lattice network model was set equal to 1 to simulate immersed conditions, while all other nodes were initialized with a user-

defined small quantity (0.01 in the reported simulations) to initiate the computation. The initial water diffusivity was set as $D_{w,0} = 0.025$ mm/min for undamaged concrete, as reported in the experiments (L. Wang & Li, 2014), while the value for the damaged lattice elements was calculated by means of Equation (9).

Figure 6(a) shows the value of the relative water content distribution (θ) with respect to depth at $t = 40$ min and $t = 80$ min estimated by the coupled LDPM approach, which fundamentally agrees with the theoretical calculations reported in the research (L. Wang & Li, 2014) using the one-dimensional unsaturated flow theory. Moreover, as shown in Figures 6(b)-(e), the simulated cumulative water content i with respect to time for concrete cubes under unstressed conditions and $0.7-0.9f_c$ stress levels align well with the experimental measurements, both in the initial and the secondary stage, thereby validating the effectiveness of the proposed two-stage relationship between water diffusivity and crack width. Additionally, Figure 7 reports θ in the elements under varying stress levels after 100, 500, and 1000 min of exposure. Results demonstrate that, when compared to the unstressed conditions, the water penetration depth in stressed concrete is significantly increased, particularly for the highest stress level for which the cracking is most pronounced.

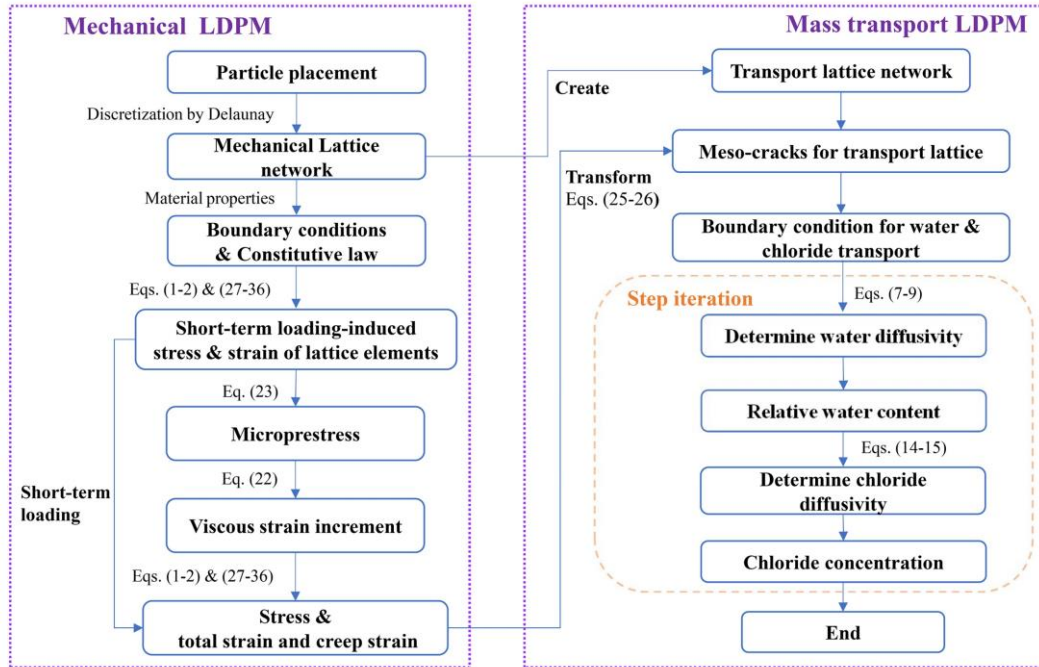


FIGURE 4 Algorithmic procedure of the developed coupled LDPM model.

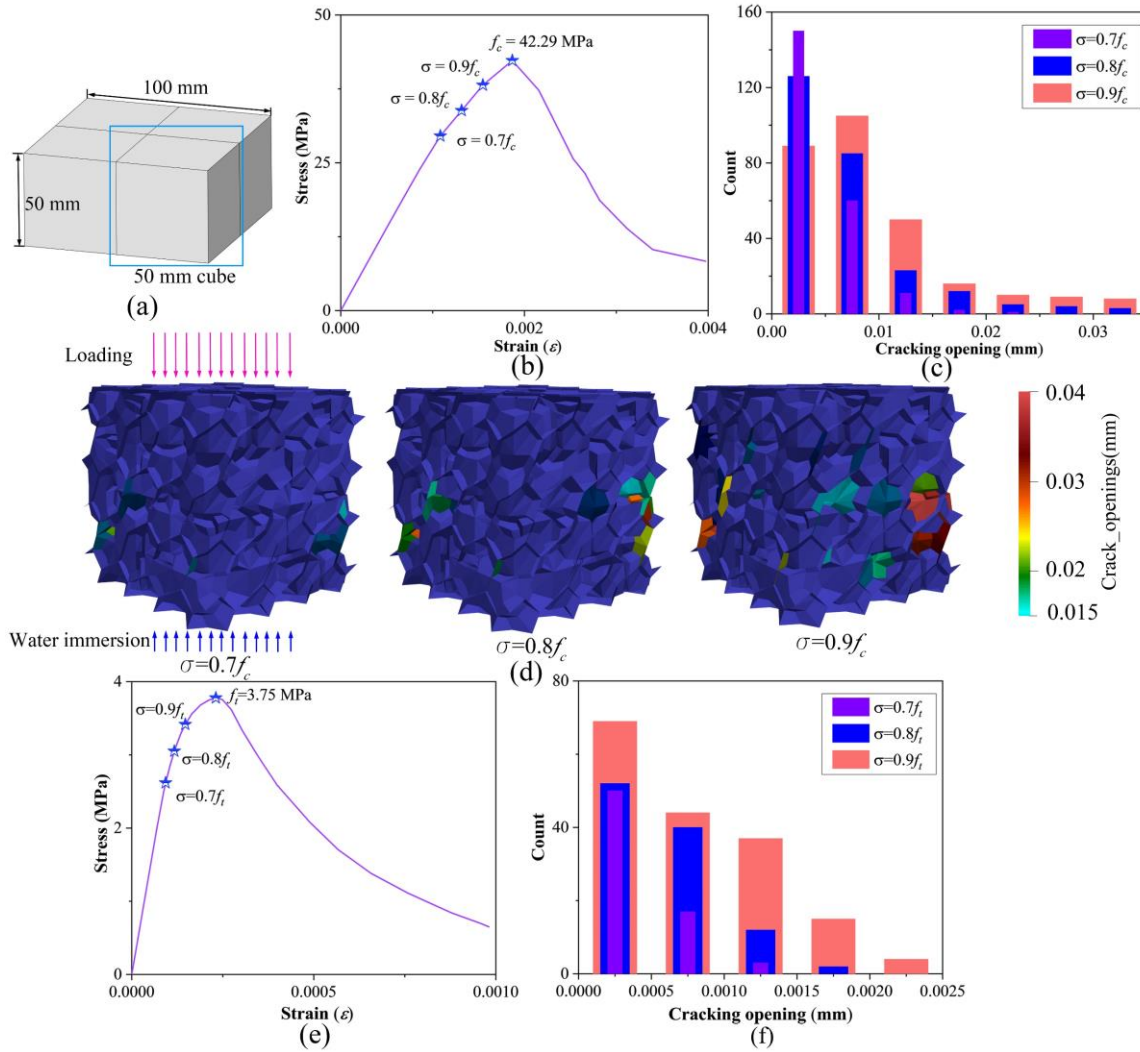


FIGURE 5 Uniaxial compressive and tensile response of concrete members: (a) experimental specimen dimension; (b) compressive stress-strain curve; (c) distribution of crack widths under different compressive stress levels; (d) crack patterns under compression; (e) tensile stress-strain curve; (f) distribution of crack widths under different tensile stress levels.

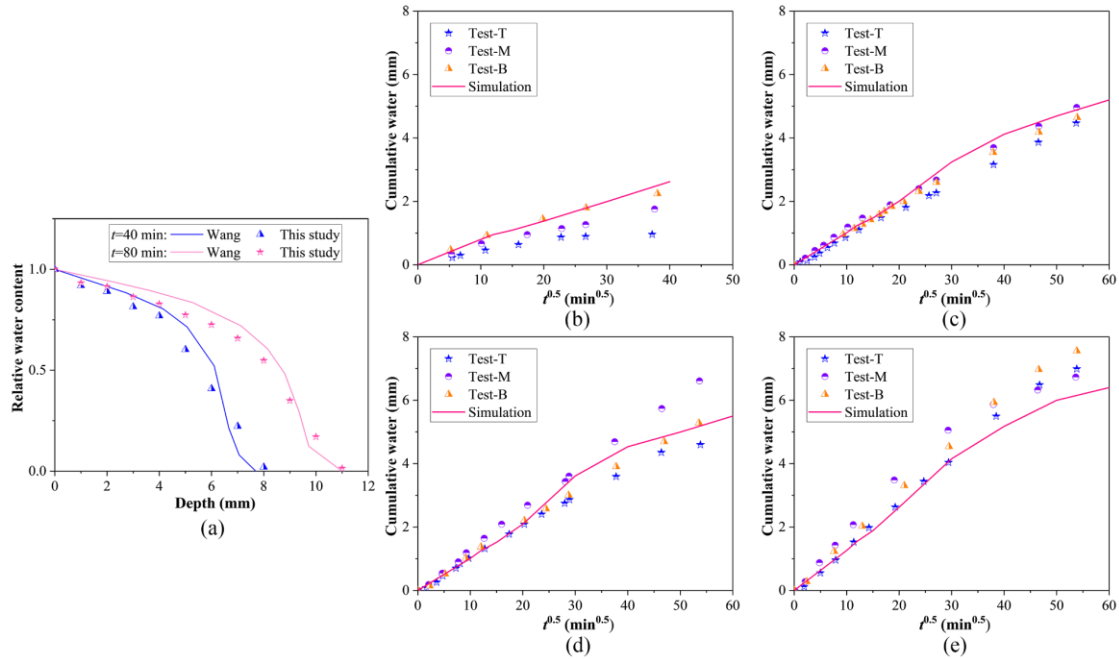


FIGURE 6 Comparison between simulated and experimental (L. Wang & Li, 2014) results: (a) water content-depth curves for unstressed conditions; cumulative water content versus \sqrt{t} curves for: (b) unstressed conditions; (c) $\sigma = 0.7f_c$; (d) $\sigma = 0.8f_c$; (e) $\sigma = 0.9f_c$.

TABLE 1 Material properties used in the different simulations reported herein.

Experiment	Model size (mm)	Aggregate size (mm)	Water/cement ratio	Young's Modulus (MPa)	ϑ	f_c (MPa)	f_t (MPa)	f_s (MPa)	G_t (N/mm ²)	G_s (N/mm ²)	n_c	n_t	ξ (MPa ⁻¹)	κ_1
Wang & Li (2014)	50×50×50	3.75~18	0.5	45000	0.25	80	3.8	9.5	0.066	0.333	0.8	2	-	-
Zhang et al. (2014)	50×50×50	3.75~20	0.46	45000	0.25	60	3.2	8.0	0.056	0.28	0.8	2	-	-
Wang et al. (2019)	300×100×100	5~10	0.43	45000	0.25	100	4.0	10.0	0.07	0.35	0.8	2	3×10^{-6}	0.002

4.2 | Water transport in concrete under tension

In a subsequent set of tests, three tensile stress levels of $0.7 \sim 0.9f_t$ were applied on the prismatic specimens to induce tensile microcracks (L. Wang & Li, 2014), with all other conditions matching the compression tests previously presented. After mechanical testing, two sub-specimens, denoted as Test-1 and Test-2, were cut from the specimens and used for immersion testing. The same LDPM discretization employed for the compression case was used to simulate the tensile testing. Figure 5(e) shows that the simulated tensile strength is approximately 3.75 MPa, which matches well with the experimental value of 3.6 ± 0.3 MPa. Figure 5(f) reports the crack width distribution in the concrete due to the various tensile stress levels. As expected, cracks

grow in both number and width as the level of the applied stress increases.

Figures 8(a)-(c) show that the computed cumulative water content versus \sqrt{t} curves for the varying tensile stress levels are in excellent agreement with the experimental measurements, further validating the applicability of the developed model. Moreover, the results demonstrate that the cumulative water content in damaged concrete is generally lower than that due to compressive loading, owing to differences in the crack distribution induced by compressive and tensile actions (see Figure 5(c) and Figure 5(f)). In addition, Figures 8(d)-(e) report the θ – depth curves under various stress levels. Similarly to the compressive tests, the water depth penetration observed in the stressed cases is significantly higher than that of the control specimen.

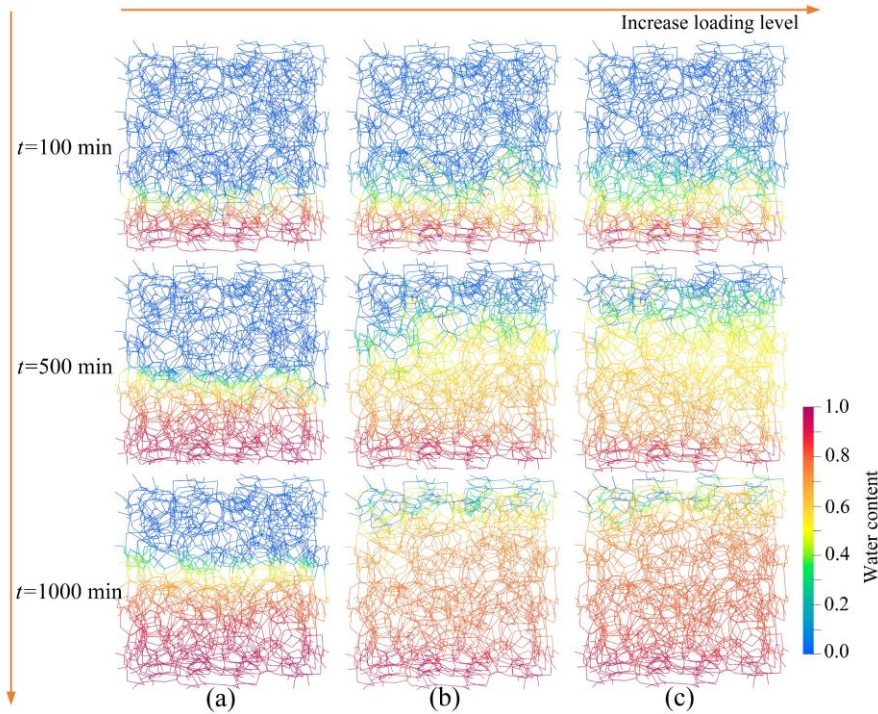


FIGURE 7 Water transport in the elements, as simulated by the developed coupled LDPM: (a) unstressed conditions; (b) $\sigma = 0.7f_c$; (c) $\sigma = 0.9f_c$.

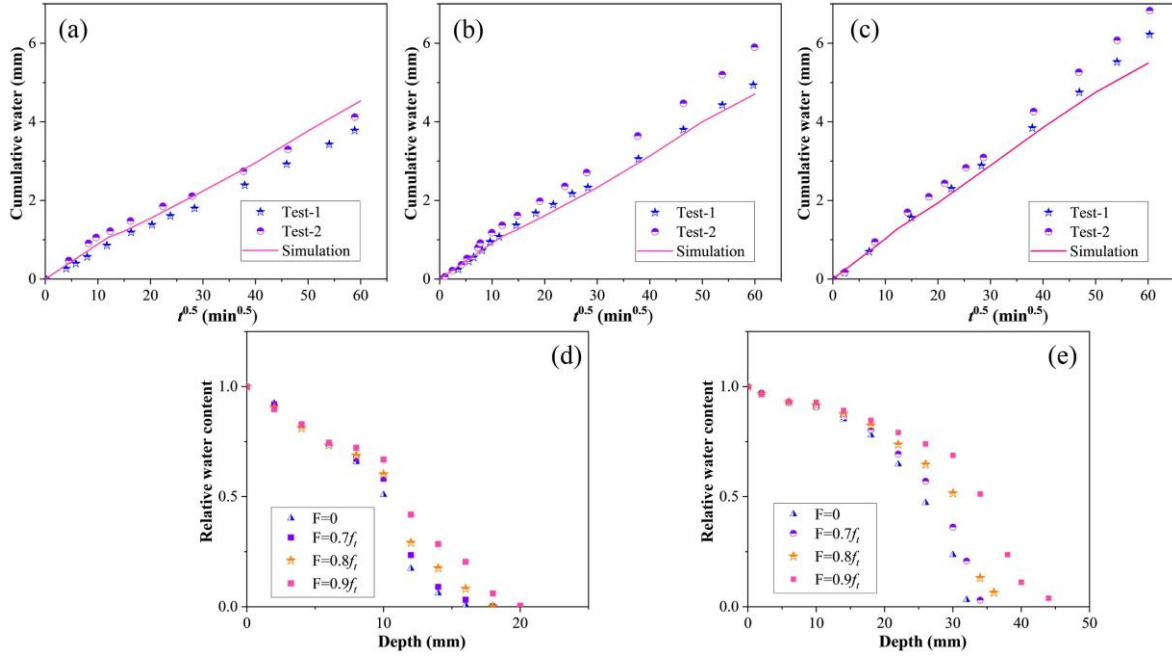


FIGURE 8 Comparison of water content in concrete under tension between simulation and experiments (L. Wang & Li, 2014): cumulative water content versus \sqrt{t} curves for: (a) $\sigma = 0.7f_t$; (b) $\sigma = 0.8f_t$; (c) $\sigma = 0.9f_t$; (d) relative water content-depth curves in specimen after 100 min exposure; (e) relative water content-depth curves in specimen after 1000 min exposure.

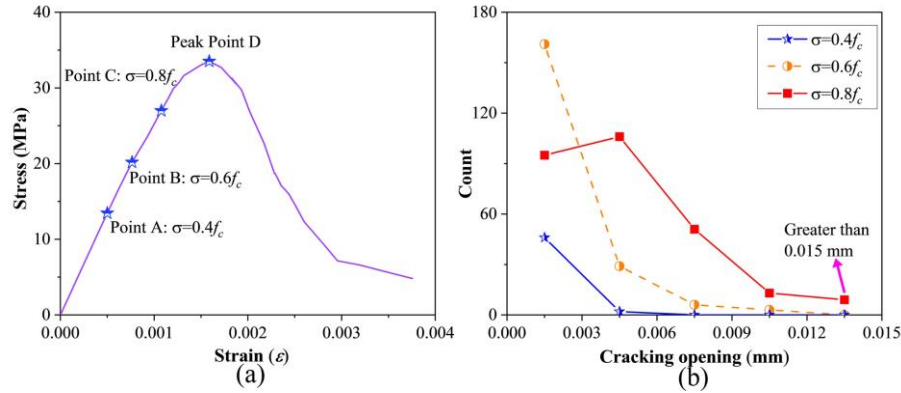


FIGURE 9 Numerical uniaxial compressive response: (a) stress-strain curve; (b) distribution of crack widths at different stress levels.

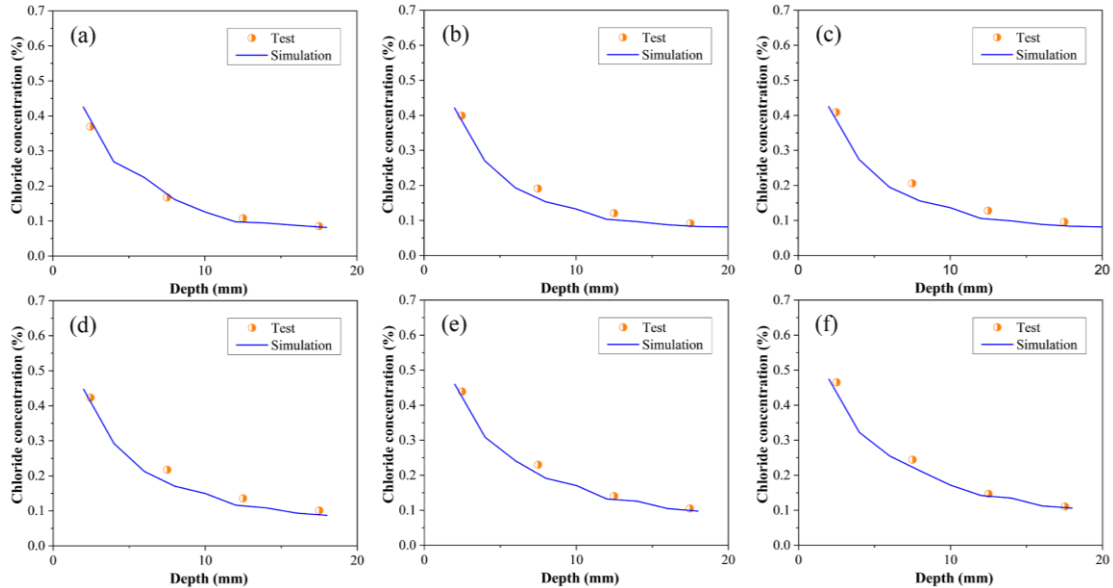


FIGURE 10 Comparison between the simulated and experimental ((L. Zhang et al., 2014)) free chloride concentration-depth curves after 56 days of exposure: (a) unstressed conditions; (b) $\sigma = 0.4f_c$; (c) $\sigma = 0.5f_c$; (d) $\sigma = 0.6f_c$; (e) $\sigma = 0.7f_c$; (f) $\sigma = 0.8f_c$.

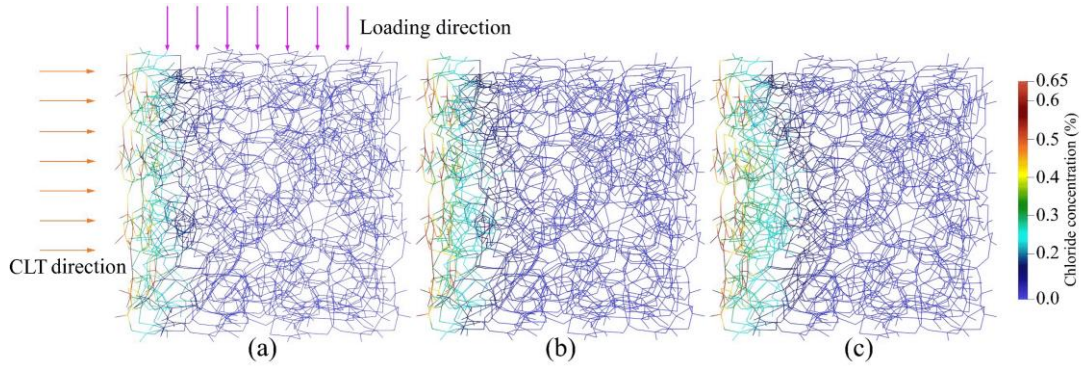


FIGURE 11 The effect of microcracks on chloride transport in concrete after 56 days of exposure: (a) unstressed conditions; (b) $\sigma = 0.6f_c$; (c) $\sigma = 0.8f_c$.

5 | NUMERICAL RESULTS CHLORIDE TRANSPORT ANALYSIS

5.1 | Chloride transport in concrete under short-term loading

L. Zhang et al., 2014 report a series of immersion tests in a solution of water and NaCl, conducted on concrete specimens with cracking induced by uniaxial compression at stress levels of $0.4 - 0.8f_c$. The reported compressive strength was 34 MPa, with a Young's modulus of 27 GPa. Similarly to the previously reported simulations, a smaller domain with a size of 50 mm was simulated to speed up computations (as diagrammed in Figure 5(a)). The boundary conditions for the uniaxial compression tests are identical to the model presented in Section 4. All the material properties employed in the simulations are again summarized in Table 1. The calibrated material properties for LDPM capture the mechanical behavior of the test specimens with satisfactory accuracy (see Figure 9(a)), with simulated values closely matching the experimental results. In addition, Figure 9(b) compares the crack width distributions for the stress conditions of $0.4f_c$ (Point A), $0.6f_c$ (Point B), and $0.8f_c$ (Point C), exhibiting the expected behavior of growing crack widths with increased loading.

In accordance with the experimental conditions, where the lateral face (perpendicular to the loading direction) of the concrete cube was exposed to the NaCl solution, the chloride concentration applied to all nodes on this face in the transport LDPM is set to 0.65%, as reported from the experiments. The chloride diffusivity for the undamaged concrete (i.e., uncracked transport lattice elements) was set to $1.0 \times 10^{-11} \text{ m}^2/\text{s}$.

Figure 10 compares the experimental and numerical free chloride concentration-depth curves after 56 days of exposure to the NaCl solution, indicating that the simulation both for the unstressed and stressed conditions closely agrees with the experimental observations. Moreover, Figure 10 demonstrates that the free chloride concentration (C_f) in concrete under the lowest stress level of $0.4f_c$ is similar to that in the unstressed case. This can be attributed to the very limited cracks observed at this level of compressive stress

(see Figure 9(b)). As the loading increases, cracking increases in both width and quantity, expanding the transport channels and forming more preferential channels, thereby accelerating CLT. In addition, Figure 11 compares the influence of stress levels on the CLT properties in concrete. As expected, C_f at the same depth becomes larger with an increase in stress level.

5.2 | Chloride transport in concrete members under long-term loading conditions

J. Wang et al., 2019 performed a series of chloride immersion tests on concrete elements under long-term 4-point bending loading conditions. The specimens have a cross-section of $100 \times 100 \text{ mm}$ and a clear span of 300 mm. In constructing the mechanical lattice network model, 1137 particles with sizes of 5~10 mm (as determined by the reported sieve curve) were randomly placed in the domain, leading to the generation of 11252 mechanical lattice elements (see Figure 12). The material properties used in the simulations are reported in Table 1. To model the 4-point bending tests, pin and roller supports were applied to the left and right bottom areas of the beam, respectively. In the simulations, a displacement-control scheme was first applied to determine the ultimate capacity (f_u), which is represented by the solid curves in Figure 12(a). Subsequently, a force-control scheme was applied to simulate the long-term loading as per the experimental protocol. Three force levels, i.e., $0.25f_u$, $0.50f_u$, and $0.75f_u$ were applied on the beam model to investigate their effects on the CLT process (see dashed lines in Figure 12(a)).

Figures 12(b)-(c) report the distribution of cracks in the beam subjected to 60 days of sustained loading. As expected, higher loading levels result in greater cracking potential, with several macroscopic cracks observed at the tension zone of the beam under the highest loading condition considered. In addition, Figure 12(b) shows the crack development of a mechanical lattice element resulting from the creep effect, indicating that cracks significantly propagate as a result of viscous effects.

In the reported experiments, the immersion tests were conducted on the pure bending region located in the middle bottom of the specimen (see Figure 12(e)), referred to as the area of interest (AOI). In this context, to improve computing

efficiency, only the nodes and transport lattice elements in the middle-bottom part of concrete beams were extracted from the overall model (red elements in Figure 12(e)) to be analyzed. Based on the experimental results, the chloride content applied to the concrete surface for the CLT simulation was set to 0.7%. The chloride diffusion coefficient for the unstressed concrete specimen was set to $0.934 \times 10^{-11} \text{ m}^2/\text{s}$ (J. Wang et al., 2019), as reported in the experiments. For the water transport analysis, the relative water content for the bottom nodes of the transport lattice network model was set to 1 to simulate full immersion.

Figure 13 reports comparison of the simulated and

experimental measurements of C_f in the specimens after 30 and 60 days of exposure. Results demonstrate that the estimated C_f curves achieve good agreement with the experimental results. Furthermore, Figure 12(f) reports the distribution of chloride concentration after 60 days of loading and exposure. The first observation is that the penetration depth for the unstressed concrete is relatively small (approximately 4 mm), whereas, for higher loading levels, the simulated value is significantly larger (approximately 8 mm). In addition, the concentration in unstressed concrete is significantly lower than that of the loaded conditions.

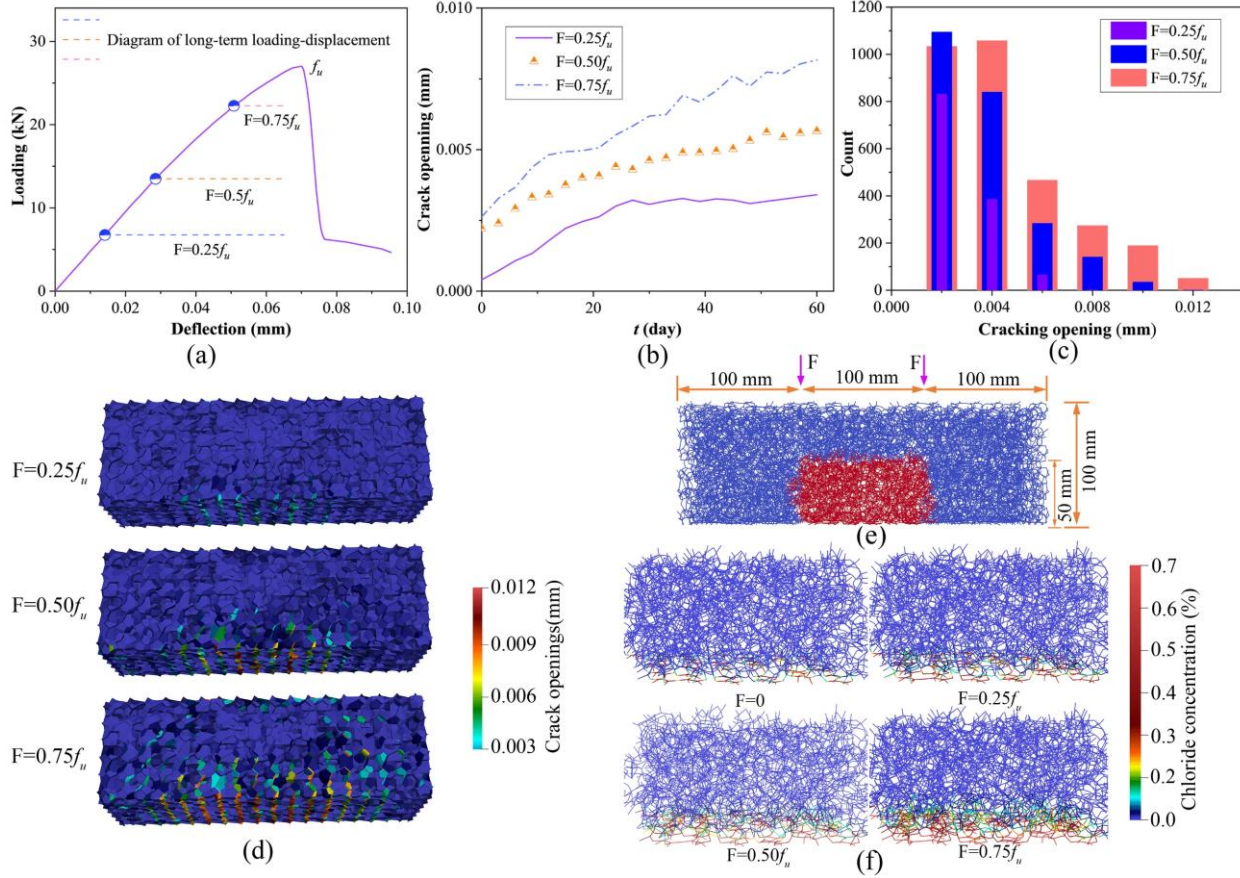


FIGURE 12 Concrete beams under long-term loadings with varying levels: (a) loading-deflection curves; (b) cracking propagation of a lattice element caused by creep effect; (c) distribution of crack width in concrete after 60 days of loadings; (d) cracking patterns after 60 days of loadings; (e) AOI (red struts) for chloride transport analysis; (f) the free chloride concentration in the AOI after 60 days of loading.

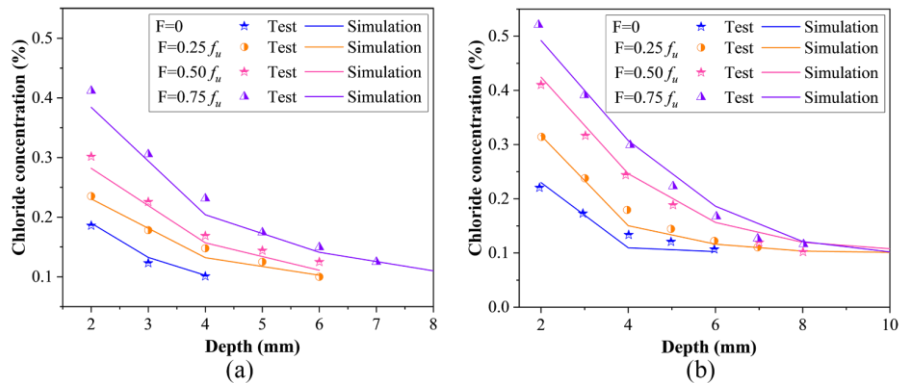


FIGURE 13 Comparison between the experimental and numerical free chloride concentration distributions after (a) 30 and (b) 60 days of loading and exposure.

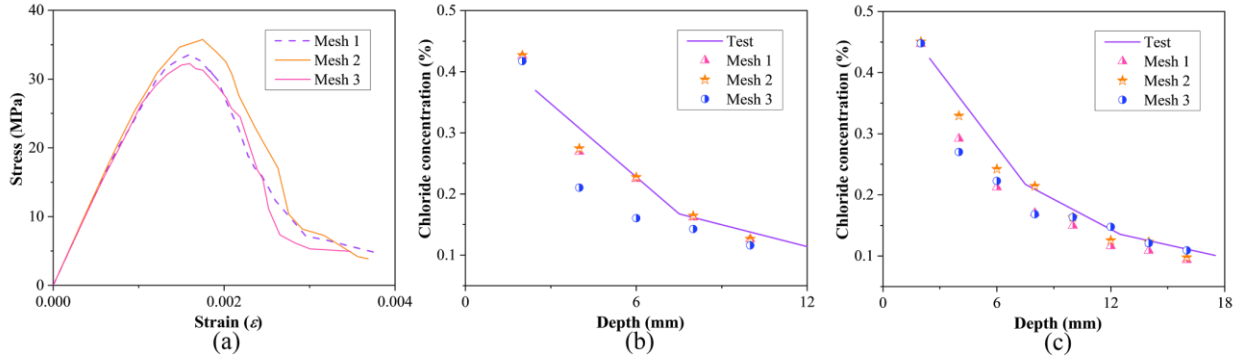


FIGURE 14 Mesh sensitivity analysis: (a) stress-strain response; (b) chloride concentration in the unstressed concrete; (c) chloride concentration in the concrete under a compressive stress level of $0.8f_c$.

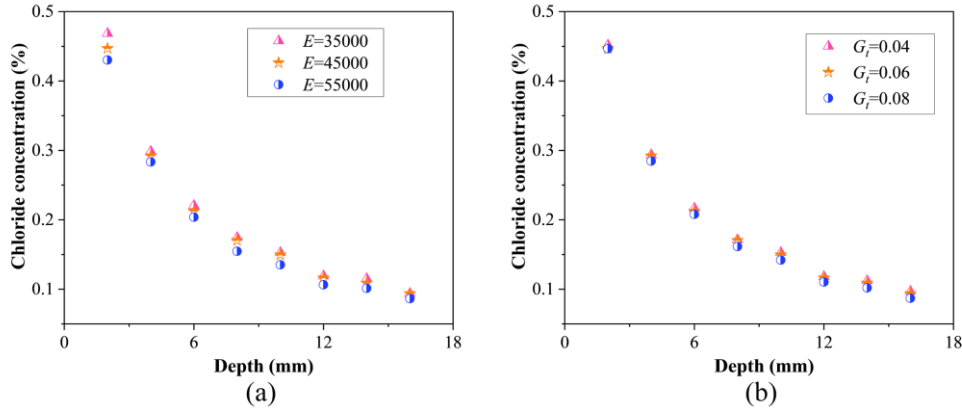


FIGURE 15 Investigation of effect of material properties on chloride transport properties: (a) Young's modulus; (b) fracture energy.

6 | DISCUSSION

6.1 | Sensitivity analysis

A mesh sensitivity analysis was conducted to demonstrate the consistency of the presented modeling approach. The same lattice network used for the results presented in Section 5.1 is denoted as Mesh 1, while two additional LDPM simulations with the same aggregate properties were generated, referred to as Mesh 2 and Mesh 3. As expected, the simulated compressive stress-strain curves of the three models are in agreement (see Figure 14(a)). Furthermore, Figures 14(b)-(c) compare the C_f – depth curves in the unstressed and stressed concrete with a loading level of $0.8f_c$. Results show that the numerical simulations are in agreement with the experimental results and with each other. The consistency among the three models with different meshes indicates that the developed model is stable with respect to the randomly generated lattice network and reliable for investigating the effect of microcracks induced by varying levels of loading on the global chloride transport properties in concrete.

In addition, the effect of material properties, such as Young's modulus and fracture energy, on chloride transport properties is investigated herein under a loading level equivalent to $0.8f_c$. For the first set of simulations, Young's modulus was selected as 35000, 45000, and 55000 MPa. In the second set of analyses, the Mode-I fracture energy G_t was varied between 0.04, 0.06, and 0.08 N/mm. As shown in

Figure 15(a), the chloride concentration after 56 days of exposure increases with decreasing Young's modulus. This is primarily because denser crack networks form as the material's stiffness is reduced. A similar pattern is observed with the change in fracture energy (see Figure 15(b)). In presence of a lower fracture energy, larger chloride concentrations occur due to the presence of denser crack networks. However, the effect of fracture energy is less significant in comparison to that of the Young's modulus.

6.2 | Effect of relative water content

In this section, the coupled LDPM approach is exercised to study the effect of the relative water content (θ) in the specimens. In particular, the following five cases were selected: $\theta = 0$ (dry condition), $\theta = 0.25$, $\theta = 0.50$, $\theta = 0.75$, and $\theta = 1$ (fully saturated condition). As reported in Figure 16, in dry environments, penetration is minimal, with a penetration depth of around 3 mm and an ion concentration of approximately 0.2% at 2 mm depth. In contrast, higher water content significantly accelerates chloride ingress, particularly in saturated conditions. For instance, penetration depth increases significantly, reaching up to 14 mm in the saturated condition. While it is expected that chloride intrusion is limited at a low water content, it is worth noting that in field conditions water solution at the outer surface of structural elements can provide a source of chloride ions. In these cases, sorption mechanisms can exacerbate chloride intrusion even when the concrete is initially dry.

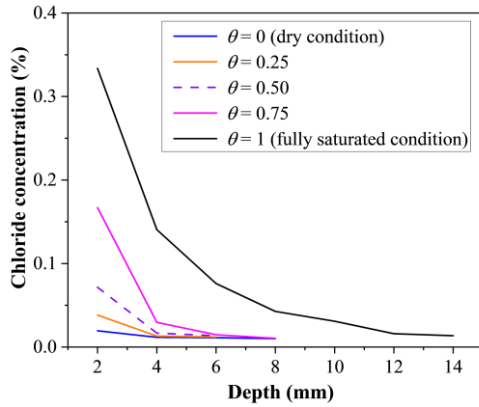


FIGURE 16 Investigation of effect of the relative water content on chloride transport properties.

6.3 | Effect of creep behavior

The model used in the 4-point bending tests, as described in Section 5.2, was also employed to study the effect of creep behavior on CLT. Figure 17 reports the C_f – depth curves under short- and long-term ($t = 60$ days) loading conditions. Results demonstrate that the free chloride concentration in the modeling scenario with considering the creep behavior is approximately 2 times larger than that of the scenario without creep behavior. Moreover, the ion penetration depth is also predicted to be significantly greater for the modeling scenario considering creep behavior. This significant acceleration of ion intrusion can be attributed to the formation of denser crack networks in the specimens with considering the viscous effects induced by long-term loading. As illustrated in Figure 12(b), cracks in the concrete for 60 days of loading increase significantly regardless of the loading magnitude, thereby widening the conduit for the transport. Therefore, the effect of creep behavior on the chloride transport analysis is expected to be significant when analyzing the transport properties of cementitious composites.

7 | CONCLUSIONS

In this study, a coupled LDPM approach was developed to describe transport properties in concrete elements subjected to short- and long-term loading conditions. A mechanical lattice was first employed to simulate crack networks induced by various types of loadings, including creep behavior under long-term loading conditions, as described by viscous strain effects in the model formulation. Such information was then mapped on a dual transport lattice network, enabling one way coupling of the cracks onto the transport properties of the lattice elements. A new formulation for the relationship

between the diffusivity coefficient and the crack width was proposed, enabling accurate assessment of the effects of cracking on the local transport properties in the material. In addition to the diffusion mechanism, the model can describe convection arising from capillary absorption. The developed model was validated by means of independent water absorption and CLT experiments on concrete members subjected to compression, tension, and 4-point bending actions. The main conclusions can be summarized as follows:

- (1) The simulation of chloride transport in cracked concrete members under different types of loading with varying stress levels agrees with the experimental results well, indicating that the developed coupled LDPM is capable of capturing the effect of cracking on the transport properties of concrete elements.
- (2) The comparison of experimental and numerical results on chloride concentrations in cracked concrete under long-term loading conditions validates the capability of the developed model to simulate the cracking propagation and mass transport properties in concrete in the presence of viscous effects.
- (3) The proposed model accurately simulates the water absorption process in concrete and effectively accounts for the impact of convection caused by water absorption on chloride transport. The simulation results indicate that relative water content significantly influences chloride transport properties by accelerating chloride diffusion.
- (4) The simulation results show that the free chloride concentration in the scenario considering creep behavior is approximately twice as high as in the scenario without creep. This indicates that creep behavior induced by long-term loading, even at lower stress levels, has a significant impact on chloride transport in concrete members.

The assumptions regarding shrinkage and viscoelastic effects on the long-term loading response provide limitations to the type of tests that can be simulated by the current implementation of the coupled LDPM model presented herein. In addition, this study primarily focused on the fundamental transport processes of diffusion and convection in cracked concrete members, while did not account for potential of wetting and drying cycles which require specific consideration and treatments such as repeated saturation and desaturation, cracking due to volume changes, and temperature-induced stresses. Based on these arguments, future work will focus on extending capabilities of the model to describe shrinkage, as well as simulating wetting and drying cycles.

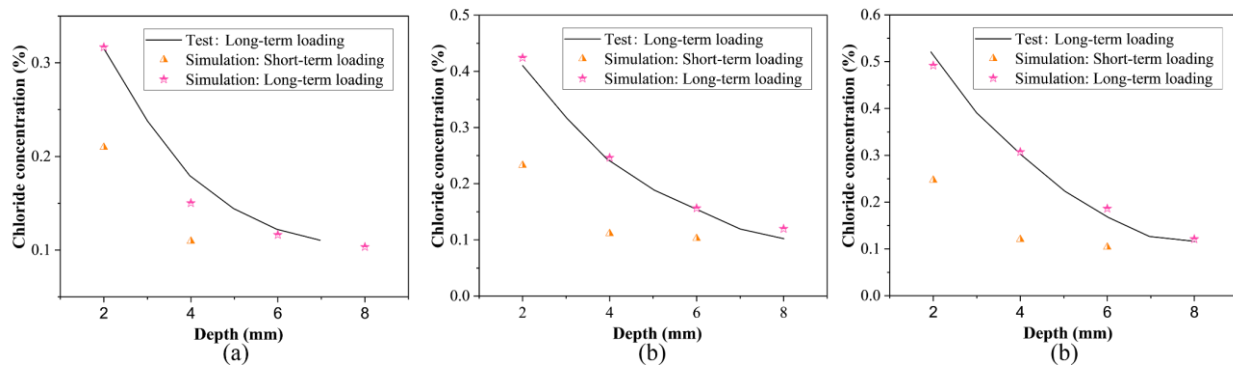


FIGURE 17 Comparison of the chloride concentration in the concrete with and without considering creep behavior: (a) $F = 0.25f_u$; (b) $F = 0.50f_u$; (c) $F = 0.75f_u$.

8 | REFERENCES

- Abdellatif, M., Boumakis, I., Wan-Wendner, R., & Alnaggar, M. (2019). Lattice Discrete Particle Modeling of concrete coupled creep and shrinkage behavior: A comprehensive calibration and validation study. *Construction and Building Materials*, 211, 629–645.
- Abyaneh, S. D., Wong, H. S., & Buenfeld, N. R. (2016). Simulating the effect of microcracks on the diffusivity and permeability of concrete using a three-dimensional model. *Computational Materials Science*, 119, 130–143.
- Adeli, H., & Kumar, S. (1995). Distributed Finite-Element Analysis on Network of Workstations—Algorithms. *Journal of Structural Engineering*, 121(10), 1448–1455.
- Bazant, Z. P., & Prasannan, S. (1989). Solidification theory for concrete creep. I: Formulation. *Journal of Engineering Mechanics*, 115(8), 1691–1703.
- Bazant, Z. P., & Prasannan, S. (1989). Solidification Theory for Concrete Creep. II: Verification and Application. *Journal of Engineering Mechanics*, 115(8), 1704–1725.
- Bentz, D. P., Garboczi, E. J., Lu, Y., Martys, N., Sakulich, A. R., & Weiss, W. J. (2013). Modeling of the influence of transverse cracking on chloride penetration into concrete. *Cement and Concrete Composites*, 38, 65–74.
- Cibelli, A., Luzio, G. Di, & Ferrara, L. (2023). Numerical Simulation of the Chloride Penetration in Cracked and Healed UHPC via a Discrete Multiphysics Model. *Journal of Engineering Mechanics*, 149(12), 5023001.
- Cusatis, G., Pelessone, D., & Mencarelli, A. (2011). Lattice Discrete Particle Model (LDPM) for failure behavior of concrete. I: Theory. *Cement and Concrete Composites*, 33(9), 881–890.
- de Vera, G., Climent, M. A., Viqueira, E., Antón, C., & Andrade, C. (2007). A test method for measuring chloride diffusion coefficients through partially saturated concrete. Part II: The instantaneous plane source diffusion case with chloride binding consideration. *Cement and Concrete Research*, 37(5), 714–724.
- Dehghan, A., Peterson, K., Riehm, G., & Herzog Bromerchenkel, L. (2017). Application of X-ray microfluorescence for the determination of chloride diffusion coefficients in concrete chloride penetration experiments. *Construction and Building Materials*, 148, 85–95.
- Dellinghausen, L. M., Gastaldini, A. L. G., Vanzin, F. J., & Veiga, K. K. (2012). Total shrinkage, oxygen permeability, and chloride ion penetration in concrete made with white Portland cement and blast-furnace slag. *Construction and Building Materials*, 37, 652–659.
- Di Luzio, G., & Cusatis, G. (2013). Solidification-microprestress-microplane (SMM) theory for concrete at early age: Theory, validation and application. *International Journal of Solids and Structures*, 50(6), 957–975.
- Djerbi Tegguer, A., Bonnet, S., Khelidj, A., & Baroghel-Bouny, V. (2013). Effect of uniaxial compressive loading on gas permeability and chloride diffusion coefficient of concrete and their relationship. *Cement and Concrete Research*, 52, 131–139.
- Fascetti, A., Bolander, J. E., & Nisticó, N. (2018). Lattice Discrete Particle Modeling of Concrete under Compressive Loading: Multiscale Experimental Approach for Parameter Determination. *Journal of Engineering Mechanics*, 144(8), 4018058.
- Fascetti, A., Ichimaru, S., & Bolander, J. E. (2022). Stochastic lattice discrete particle modeling of fracture in pervious concrete. *Computer-Aided Civil and Infrastructure Engineering*, 37(14), 1788–1808.
- Fascetti, A., & Oskay, C. (2019). Dual random lattice modeling of backward erosion piping. *Computers and Geotechnics*, 105, 265–276.
- Federal Highway Administration. (2002). *Corrosion Cost and Preventive Strategies in the United States*.
- Grassl, P. (2009). A lattice approach to model flow in cracked concrete. *Cement and Concrete Composites*, 31(7), 454–460.
- Grassl, P., & Bolander, J. (2016). Three-Dimensional Network Model for Coupling of Fracture and Mass Transport in Quasi-Brittle Geomaterials. *Materials*, 9(9).
- Hafezolzhorani, M., Hejazi, F., Jaffar, M. S., & Adeli, H. (2022). Plasticity model for partially prestressed concrete. *Structures*, 38, 630–651. <https://www.sciencedirect.com/science/article/pii/S2352012422000996>
- Hall, C. (1989). Water sorptivity of mortars and concretes: a review. *Magazine of Concrete Research*, 41(147), 51–61.
- Ismail, M., Toumi, A., François, R., & Gagné, R. (2004). Effect of crack opening on the local diffusion of chloride in inert materials. *Cement and Concrete Research*, 34(4), 711–716.
- Jang, S. Y., Kim, B. S., & Oh, B. H. (2011). Effect of crack width on chloride diffusion coefficients of concrete by steady-state migration tests. *Cement and Concrete Research*, 41(1), 9–19.

- <https://doi.org/https://doi.org/10.1016/j.cemconres.2010.08.018>
- Jia, D., Brigham, J. C., & Fascetti, A. (2024). An efficient static solver for the lattice discrete particle model. *Computer-Aided Civil and Infrastructure Engineering*.
- Li, W., & Guo, L. (2020). A mechanical-diffusive peridynamics coupling model for meso-scale simulation of chloride penetration in concrete under loadings. *Construction and Building Materials*, 241.
- Lim, C. C., Gowripalan, N., & Sirivivatnanon, V. (2000). Microcracking and chloride permeability of concrete under uniaxial compression. *Cement and Concrete Composites*, 22(5), 353–360.
- Liu, J., Ou, G., Qiu, Q., Chen, X., Hong, J., & Xing, F. (2017). Chloride transport and microstructure of concrete with/without fly ash under atmospheric chloride condition. *Construction and Building Materials*, 146, 493–501.
- Liu, Q., Hu, Z., Wang, X., Zhao, H., Qian, K., Li, L. jie, & Meng, Z. (2022). Numerical study on cracking and its effect on chloride transport in concrete subjected to external load. *Construction and Building Materials*, 325.
- Lockington, D. (1993). Estimating the Sorptivity for a Wide Range of Diffusivity Dependence on Water Content. In *Transport in Porous Media* (Vol. 10). Kluwer Academic Publishers.
- Lockington, D., Parlange, J.-Y., & Dux, P. (1999). Sorptivity and the estimation of water penetration into unsaturated concrete. *Materials and Structures*, 32, 342–347.
- Marsavina, L., Audenaert, K., De Schutter, G., Faur, N., & Marsavina, D. (2009). Experimental and numerical determination of the chloride penetration in cracked concrete. *Construction and Building Materials*, 23(1), 264–274.
- <https://doi.org/10.1016/j.conbuildmat.2007.12.015>
- Peng, J., Hu, S., Zhang, J., Cai, C. S., & Li, L. yuan. (2019). Influence of cracks on chloride diffusivity in concrete: A five-phase mesoscale model approach. *Construction and Building Materials*, 197, 587–596.
- Qiu, Q., & Dai, J.-G. (2021). Meso-scale modeling of chloride diffusivity in mortar subjected to corrosion-induced cracking. *Computer-Aided Civil and Infrastructure Engineering*, 36(5), 602–619.
- Quqa, S., Landi, L., & Loh, K. J. (2023). Crack identification using electrical impedance tomography and transfer learning. *Computer-Aided Civil and Infrastructure Engineering*, 38(17), 2426–2442.
- Rafiei, M. H., Khushefati, W. H., Demirboga, R., & Adeli, H. (2016). Neural Network, Machine Learning, and Evolutionary Approaches for Concrete Material Characterization. *ACI Materials Journal*, 113(6).
- Rafiei, M. H., Khushefati, W. H., Demirboga, R., & Adeli, H. (2017a). Novel Approach for Concrete Mixture Design Using Neural Dynamics Model and Virtual Lab Concept. *ACI Materials Journal*, 114(1).
- Rafiei, M. H., Khushefati, W. H., Demirboga, R., & Adeli, H. (2017b). Supervised deep restricted Boltzmann machine for estimation of concrete. *ACI Materials Journal*, 114(2), 237.
- Rahman, M. K., Al-Kutti, W. A., Shazali, M. A., & Baluch, M. H. (2012). Simulation of Chloride Migration in Compression-Induced Damage in Concrete. *Journal of Materials in Civil Engineering*, 24(7), 789–796.
- Saeki, T., & Niki, H. (1996). Migration of chloride ions in non-saturated mortar. 963–968.
- Şahmaran, M. (2007). Effect of flexure induced transverse crack and self-healing on chloride diffusivity of reinforced mortar. *Journal of Materials Science*, 42(22), 9131–9136.
- Šavija, B., Luković, M., & Schlangen, E. (2014). Lattice modeling of rapid chloride migration in concrete. *Cement and Concrete Research*, 61–62, 49–63.
- Šavija, B., Pacheco, J., & Schlangen, E. (2013). Lattice modeling of chloride diffusion in sound and cracked concrete. *Cement and Concrete Composites*, 42, 30–40.
- Shen, L., Li, W., Zhou, X., Feng, J., Di Luzio, G., Ren, Q., & Cusatis, G. (2020). Multiphysics Lattice Discrete Particle Model for the simulation of concrete thermal spalling. *Cement and Concrete Composites*, 106, 103457.
- Tong, L., Liu, Q., Xiong, Q., Meng, Z., Amiri, O., & Zhang, M. (2024). Modeling the chloride transport in concrete from microstructure generation to chloride diffusivity prediction. *Computer-Aided Civil and Infrastructure Engineering*.
- Tran, T. T., Pham, D. T., Vu, M. N., Truong, V. Q., Ho, X. B., Tran, N. L., Nguyen-Sy, T., & To, Q. D. (2021). Relation between water permeability and chloride diffusivity of concrete under compressive stress: Experimental investigation and mesoscale lattice modelling. *Construction and Building Materials*, 267.
- Wang, J., Basheer, P. A. M., Nanukuttan, S. V., Long, A. E., & Bai, Y. (2016). Influence of service loading and the resulting micro-cracks on chloride resistance of concrete. *Construction and Building Materials*, 108, 56–66.
- <https://www.sciencedirect.com/science/article/pii/S0950061816300058>
- Wang, J., Niu, D., Wang, Y., He, H., & Liang, X. (2019). Chloride diffusion of shotcrete lining structure subjected to nitric acid, salt–frost degradation, and bending stress in marine environment. *Cement and Concrete Composites*, 104.
- Wang, L., Bao, J., & Ueda, T. (2016). Prediction of mass transport in cracked-unsaturated concrete by mesoscale lattice model. *Ocean Engineering*, 127, 144–157.
- Wang, L., & Li, S. (2014). Capillary absorption of concrete after mechanical loading. *Magazine of Concrete Research*, 66(8), 420–431.
- Wang, L., & Ueda, T. (2014). Mesoscale Modeling of Chloride Penetration in Unsaturated Concrete Damaged by Freeze-Thaw Cycling. *Journal of Materials in Civil Engineering*, 26(5), 955–965.
- Wang, Z., Oskay, C., & Fascetti, A. (2024). Three-dimensional numerical modeling of the temporal evolution of backward erosion piping. *Computers and Geotechnics*, 171, 106381.
- Xi, Y., & Bažant, Z. P. (1999). Modeling Chloride Penetration in Saturated Concrete. *Journal of Materials in Civil Engineering*, 11(1), 58–65.
- Yang, Z., Weiss, W. J., & Olek, J. (2006). Water Transport in Concrete Damaged by Tensile Loading and Freeze-Thaw Cycling. *Journal of Materials in Civil Engineering*, 18(3), 424–434.

- Ye, W., Ren, J., Zhang, A. A., & Lu, C. (2023). Automatic pixel-level crack detection with multi-scale feature fusion for slab tracks. *Computer-Aided Civil and Infrastructure Engineering*, 38(18), 2648–2665.
- Yin, H., Cibelli, A., Brown, S.-A., Yang, L., Shen, L., Alnaggar, M., Cusatis, G., & Di Luzio, G. (2024). Flow lattice model for the simulation of chemistry dependent transport phenomena in cementitious materials. *European Journal of Environmental and Civil Engineering*, 28(5), 1039–1063.
- Yu, G., & Adeli, H. (1993). Object-Oriented Finite Element Analysis Using EER Model. *Journal of Structural Engineering*, 119(9), 2763–2781. [https://doi.org/10.1061/\(ASCE\)0733-9445\(1993\)119:9\(2763\)](https://doi.org/10.1061/(ASCE)0733-9445(1993)119:9(2763))
- Zhang, L., Jia, J., Meng, G., & Zhu, W. (2014). Chloride diffusion in concrete subjected to compressive loading. *Magazine of Concrete Research*, 66(19), 991–997.
- Zhang, Y., Luzio, G. Di, & Alnaggar, M. (2021). Coupled multi-physics simulation of chloride diffusion in saturated and unsaturated concrete. *Construction and Building Materials*, 292, 123394.
- Zhang, Y. S., Sun, W., Liu, Z. Y., & Chen, S. D. (2011). One and two dimensional chloride ion diffusion of fly ash concrete under flexural stress. *Journal of Zhejiang University: Science A*, 12(9), 692–701.
- Zhang, Y., Zhang, M., & Ye, G. (2018). Influence of moisture condition on chloride diffusion in partially saturated ordinary Portland cement mortar. *Materials and Structures/Materiaux et Constructions*, 51(2).
- Zheng, B., Li, T., Qi, H., Gao, L., Liu, X., & Yuan, L. (2022). 3D meso-scale simulation of chloride ion transportation in cracked concrete considering aggregate morphology. *Construction and Building Materials*, 326.
- Zhou, Z., Zhang, J., & Gong, C. (2023). Hybrid semantic segmentation for tunnel lining cracks based on Swin Transformer and convolutional neural network. *Computer-Aided Civil and Infrastructure Engineering*, 38(17), 2491–2510.
- Zhu, Y., & Fascetti, A. (2024). Towards Developing Reinforced Concrete Structures Digital Twins: A Multiscale Lattice Discrete Particle Model Approach. *Advances in Structural Engineering*.
- Zhu, Y., Fascetti, A., Giesler, S., Murru, P., & Grasley, Z. (2024). Regularized Density-Driven Damage Mechanics Model for Failure Analysis of Cementitious Composites. *Journal of Engineering Mechanics*, 150(9), 4024064.

Appendix

At the elastic stage, the normal and tangential tractions are defined as:

$$\begin{cases} \sigma_n = E_n \varepsilon_n^{IJ} \\ \sigma_t = E_t \varepsilon_t^{IJ} = \vartheta E_n \varepsilon_t^{IJ} \end{cases} \quad (27)$$

where ε_n^{IJ} and $\varepsilon_t^{IJ} = \sqrt{\varepsilon_l^{IJ^2} + \varepsilon_m^{IJ^2}}$ are the normal and tangential strain measures of each lattice element, respectively; E_n and $E_t = \vartheta E_n$ are the lattice-level normal and shear moduli, respectively.

The elliptical bounding surface defined to describe the elastic boundary of lattice strut is formulated as a function of the compressive (f_c), tensile (f_t) and shear (f_s) stress limits:

$$\sigma_n(\sigma_n - f_c - f_t) - \frac{f_c f_t}{f_s^2} \sigma_t^2 + f_c f_t = 0 \quad (28)$$

The softening behavior of the lattice element is defined as:

$$\sigma_b(\omega) = \sigma_0 e^{\frac{-H}{\sigma_0} \langle \varepsilon_1 - \varepsilon_0 \rangle} \quad (29)$$

$$H(\omega) = H_s + (H_t - H_s) \left(\frac{2\omega}{\pi} \right)^{n_t} \quad (30)$$

$$H_s = H(\omega = 0) = \frac{2E_t}{(2E_t G_s)/(f_s^2 l^e) - 1} \quad (31)$$

$$H_t = H\left(\omega = \frac{\pi}{2}\right) = \frac{2E_n}{(2E_n G_t)/(f_t^2 l) - 1} \quad (32)$$

where σ_0 and ε_0 are the effective traction and strain measures at the elastic limit; ε_1 is a history-dependent measure of maximum effective strain attained in each element, simulating damage irreversibility; H is the exponential softening modulus, which is defined as a function of the length l , the Mode-I fracture energy G_t and Mode-II fracture energy G_s , to correctly preserve the mesoscopic level energy; H_t is the softening modulus under pure tensile loading ($w = \pi/2$), and H_s is the softening modulus under pure shear condition ($w = 0$). A smooth transition for the parameter H is considered for a mixed-mode fracture, employing the exponential coefficient n_t .

The compressive hardening behavior of the lattice element is given:

$$\sigma = \begin{cases} f_c & \varepsilon_v \geq 0 \\ f_c e^{\frac{H}{f_c} (-\varepsilon_v - \varepsilon_c)} & \varepsilon_v < 0 \end{cases} \quad (33)$$

$$H = \frac{H_c}{1 + \frac{\varepsilon_v}{\varepsilon_D}} \quad (34)$$

where H is the hardening modulus for the compression case; H_c is a material parameter, representing the hardening modulus under no volumetric strain; ε_D is the deviatoric strain at a lattice strut; ε_c is the strain corresponding to the compressive limit stress.

The frictional behavior of the lattice element is expressed as:

$$\sigma = \sigma_{t,0} e^{\frac{-H}{\sigma_{t,0}} \langle \varepsilon_t - \varepsilon_{t,0} \rangle} \quad (35)$$

$$H = H_s - H_s \left(\frac{-2\omega}{\pi} \right)^{n_c} \quad (36)$$

where $\sigma_{t,0}$ and $\varepsilon_{t,0}$ are the tangential traction and strain of a lattice strut at the elastic limit; H is the softening shear modulus; n_c is a material parameter that governs the transition from a pure shear state to a pure compressive state.